The two Titan stellar occultations of 14 November 2003

B. Sicardy,[1] F. Colas,[2] T. Widemann,[1] A. Bellucci,[1] W. Beisker,[3] M. Kretlow,[3] F. Ferri,[4]
S. Lacour,[1] J. Lecacheux,[1] E. Lellouch,[1] S. Pau,[1] S. Renner,[1] F. Roques,[1] A. Fienga,[2]
C. Etienne,[5] C. Martinez,[6] I. S. Glass,[7] D. Baba,[8] T. Nagayama,[8] T. Nagata,[8]
S. Itting-Enke,[9] K.-L. Bath,[3] H.-J. Bode,[3] F. Bode,[3] H. Lüdemann,[3] J. Lüdemann,[3]
D. Neubauer,[3] A. Tegtmeier,[3] C. Tegtmeier,[3] B. Thomé,[3] F. Hund,[10] C. deWitt,[11]
B. Fraser,[11] A. Jansen,[11] T. Jones,[11] P. Schoenau,[11] C. Turk,[11] P. Meintjies,[12]
M. Hernandez,[13] D. Fiel,[14] E. Frappa,[15] A. Peyrot,[16] J. P. Teng,[16] M. Vignand,[16]
G. Hesler,[17] T. Payet,[17] R. R. Howell,[18] M. Kidger,[19] J. L. Ortiz,[20] O. Naranjo,[21]
P. Rosenzweig,[21] and M. Rapaport[22]

[1]   We report the observation of two stellar occultations by Titan on 14 November 2003, using stations in the Indian Ocean, southern Africa, Spain, and northern and southern Americas. These occultations probed altitudes between ~550 and 250 km (~1 to 250 μbar) in Titan's upper stratosphere. The light curves reveal a sharp inversion layer near 515 ± 6 km altitude (1.5 μbar pressure level), where the temperature increases by 15 K in only 6 km. This layer is close to an inversion layer observed fourteen months later by the Huygens HASI instrument during the entry of the probe in Titan's atmosphere on 14 January 2005 [Fulchignoni et al., 2005]. Central flashes observed during the first occultation provide constraints on the zonal wind regime at 250 km, with a strong northern jet (~200 m s^{-1}) around the latitude 55°N, wind velocities of ~150 m s^{-1} near the equator, and progressively weaker winds as more southern latitudes are probed. The haze distribution around Titan's limb at 250 km altitude is close to that predicted by the Global Circulation Model of Rannou et al. (2004) in the southern hemisphere, but a clearing north of 40°N is necessary to explain our data. This contrasts with Rannou et al.'s (2004) model, which predicts a very thick polar hood over Titan's northern polar regions. Simultaneous observations of the flashes at various wavelengths provide a dependence of $\tau \propto \lambda^{-q}$, with $q = 1.8 \pm 0.5$ between 0.51 and 2.2 μm for the tangential optical depth of the hazes at 250 km altitude.

Citation: Sicardy, B., et al. (2006), The two Titan stellar occultations of 14 November 2003, *J. Geophys. Res.*, *111*, E11S91, doi:10.1029/2005JE002624.

1. Introduction

[2]   On 14 November 2003, Titan occulted two bright stars of the Tycho catalog: TYC 1343-1615-1 (V = 8.6) and TYC 1343-1865-1 (V = 10.7). The first occultation was visible right after midnight (UT) from the Indian Ocean and the southern half of Africa, while the second one was observable about seven hours later from western Europe,

[1]Observatoire de Paris, LESIA, Meudon, France.
[2]Observatoire de Paris, IMCCE, Paris, France.
[3]International Occultation Timing Association, European Section, Hannover, Germany.
[4]CISAS "G. Colombo", Università di Padova, Padova, Italy.
[5]Observatoire de Paris, CERCOM, Meudon, France.
[6]Instituto Superior de Ciencias Astronómicas, and Liga Iberoamericana de Astronomía, Buenos Aires, Argentina.
[7]South African Astronomical Observatory, Cape Town, South Africa.
[8]Department of Astrophysics, Nagoya University, Nagoya, Japan.
[9]Windhoek, Namibia.
[10]Hakos Guestfarm, Windhoek, Namibia.
[11]Astronomical Society of Southern Africa, South Africa.

[12]Boyden Observatory, University of the Free State, Bloemfontein, South Africa.
[13]Association Aude, Paris, France.
[14]Lycée Stanislas, Paris, France.
[15]Astronef, Planétarium de Saint-Etienne, Saint-Etienne, France.
[16]Observatoire Les Makes, La Rivière, La Réunion, France.
[17]ARECA, Sainte-Marie, La Réunion, France.
[18]Wyoming InfraRed Observatory, Department of Physics and Astronomy, Laramie, Wyoming, USA.
[19]Instituto de Astrofisica de Canarias, La Laguna, Tenerife, Spain.
[20]Instituto de Astrofisica de Andalucía, Granada, Spain.
[21]Universidad de Los Andes, Facultad de Ciencias, Departamento de Física, Grupo de Astrofísica Teórica, Mérida, Venezuela.
[22]Observatoire Aquitain des Sciences de l'Univers, Floirac, France.
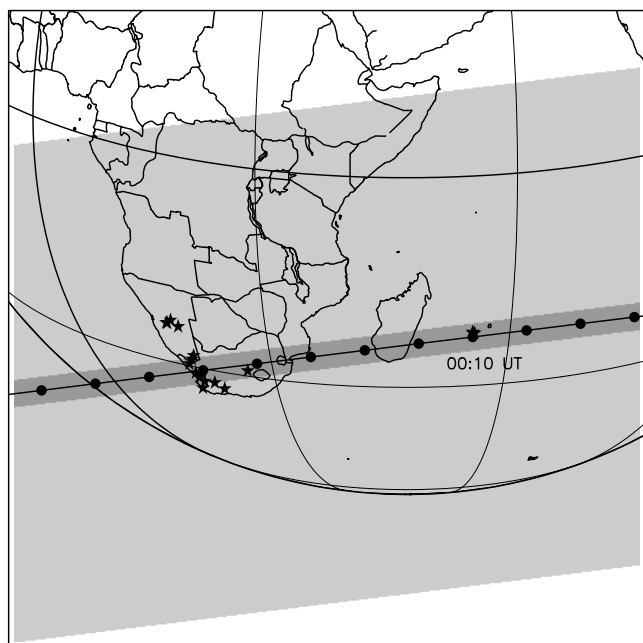
Figure 1. Reconstruction of Titan's shadow trajectory on the Earth for occultation 1; see section 3.3 for details. The size of the map is 8000 × 8000 km. The dots on the shadow central line are plotted every minute, and the shadow is moving from right to left. The light gray band represents the projection of a radius of 3100 km at Titan, corresponding to the highest stratospheric zones detectable with ground-based stellar occultations. It corresponds to an altitude of ~525 km and a pressure of ~0.8 μbar in Titan's atmosphere. The darker central band indicates the region where the central flash could be detected. The star symbols locate the sites where observations were attempted, on La Réunion Island (coincident with the dot marking the shadow center at 00:10 UT), in the Republic of South Africa and in Namibia; see Figure 2 for details.

the Atlantic Ocean, and northern and central Americas; see Figures 1, 2, and 3.

[3] These two events were predicted by one of us (C. Martinez) in October 2002, and were subsequently announced by D. Dunham and D. Herald (personal communications, 2003). Such events are rare, and the fact that two of them were observed during the same night is purely fortuitous. The previously observed occultations by Titan occurred on 3 July 1989 [see, e.g., *Hubbard et al.*, 1993; *Sicardy et al.*, 1999], on 21 August 1995 [*Tracadas et al.*, 2001], and on 20 December 2001 [*Bouchez*, 2004].

[4] The two occultations of November 2003 were unique opportunities to probe Titan's upper stratosphere seven months before the insertion of the Cassini/Huygens spacecraft into the Saturnian system (2 July 2004), and fourteen months before the entry of the Huygens probe into Titan's atmosphere (14 January 2005).

[5] We organized a campaign to observe both events with the aid of professional and amateur astronomers. The main goals were to do the following:

[6] 1. Probe Titan's upper stratosphere from altitude levels of ~600 km (~0.1 μbar) down to ~250 km (~250 μbar) with unprecedented km resolution, as the stellar disks had apparent diameters of about 2.2 and 0.84 km for the two occultations, respectively, when projected at Titan's distance.

[7] 2. Detect the central flash from various stations in order to reconstruct the 250 μbar isobar shape (at ~250 km altitude) and then derive the zonal wind regime at that level.

[8] 3. Use the attenuation of the stellar fluxes during the occultations to derive the optical depths of aerosols at various wavelengths, from ~0.5 to 2.2 μm.

[9] 4. Compare these results to what was derived from the 28 Sgr event of July 1989. The time span between July 1989 and November 2003 corresponds to about half of a Titanian year, so that the reversal of seasonal effects can be detected with these experiments.

[10] 5. Compare our results with those derived by the Huygens probe during its entry in Titan's atmosphere on 14 January 2005, and more generally, by the Cassini orbiter during its mission around Saturn from 2004 to 2008.

[11] In this paper, we focus on the first occultation, which was observed by more stations and yielded a central flash detection. However, the occultation light curves of the second occultation are also shown in Figures 4 and 5 for completeness, and the timing of this occultation is used for the astrometric reconstruction of the events; see section 3.3. This paper addresses the global properties of the atmosphere: (1) presence of an ubiquitous inversion layer near the 515 km altitude level, (2) zonal wind regime at 250 km, and (3) large-scale haze distribution and chromatic extinction, also at 250 km. In another paper in preparation (referred to as Paper 2 hereafter), we will present a detailed comparison of all the light curves, with an analysis of the fine-scale structures observed during both the ingress, egress and central flash parts of the light curves.

2. Observations

[12] The occultation light curves are displayed in Figure 4 and the circumstances of observations are summarized in Table 1. This table also gives the acronyms used in this paper to designate the various stations involved in this campaign. The observations were made with both small portable telescopes, and larger, fixed instruments. All data were recorded on 2-D arrays which imaged the two events, except for the SAAO station, where an aperture photometer was used.

[13] Filters were chosen for those instruments with sufficient signal-to-noise ratio (SNR), while clear, broad band observations were made with smaller telescopes in order to maximize photon flux. After convolving the receptor spectral responses with the bands used for each experiment, we obtain effective wavelengths of 0.51, 0.70, 0.81, 0.89 (I band) and 2.2 (K band) μm for the various occultation light curves. These multiwavelength observations allow us to probe the Titan aerosol opacity over a wide interval. In particular, they extend to the near IR the observations made during the 28 Sgr occultation in 1989, which were made between 0.45 and 0.89 μm [*Hubbard et al.*, 1993].

[14] A bonus of the 14 November 2003 events was the small angular sizes of the occulted stars. These sizes are
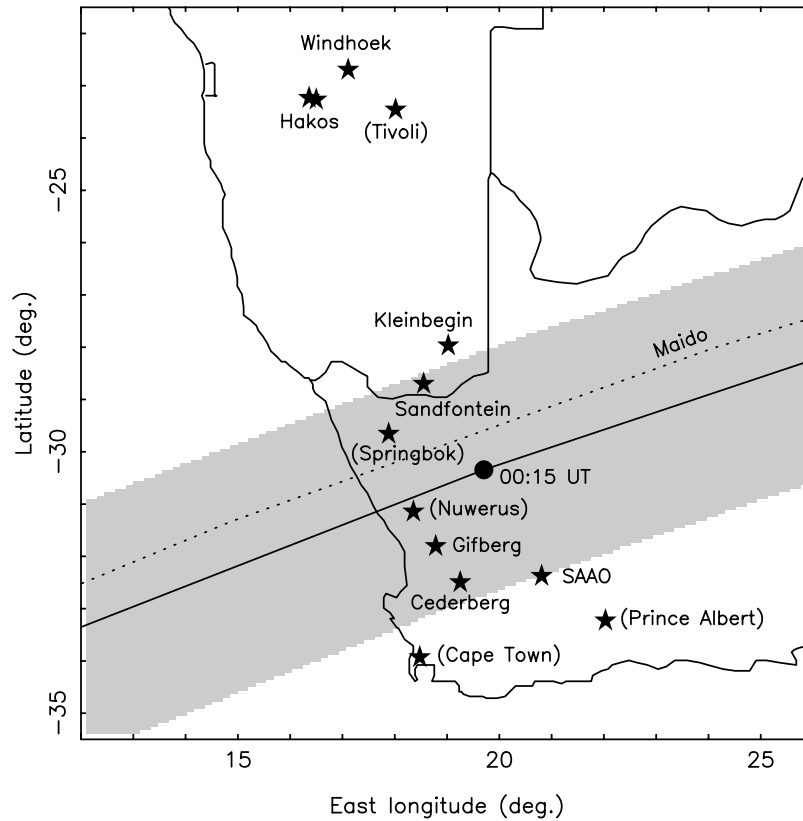
Figure 2. Detail of the central flash region over southern Africa. In this enlargement of Figure 1, the trajectory of the central flash (gray band) is plotted in a longitude-latitude map. The star symbols show all the sites where observations were attempted, the stations in parentheses corresponding to the sites where no data were gathered, due to weather or detector problems. The central flash region drawn here is approximate, as the central flash was not symmetric with respect the the shadow center; see Figure 12. The dotted line indicates the relative offset to centrality probed by the Maïdo station in La Réunion Island; see Figure 1.

estimated by using the formulae of *van Belle* [1999] for giant and supergiant stars, with quoted errors of 10%. For both stars, we used the magnitudes provided by the Vizier site http://vizier.u-strasbg.fr/cgi-bin/VizieR). For the first star (TYC 1343-1615-1), we obtain: $m_B = 9.87$, $m_V = 8.56$, $m_J = 6.50$, $m_H = 5.97$, $m_K = 5.84$, from which we derive an angular size of 0.36 mas, corresponding to 2.2 km when projected at Titan. For the second star (TYC 1343-1865-1), we have: $m_B = 11.9$, $m_V = 10.7$, $m_J = 8.60$, $m_H = 8.08$, $m_K = 7.95$, from which we get an angular size of 0.14 mas, corresponding to 0.84 km projected at Titan. Note, however, that during an occultation, the differential refraction shrinks the star diameter perpendicular to Titan's limb proportionally to the flux. Thus, below the half-light levels, subkilometer vertical resolutions were attained for both occultations.

[15] Note also that these angular sizes are one order of magnitude smaller than that of 28 Sgr, occulted by Titan on 3 July 1989, whose diameter was estimated to 18.5 km when projected at the satellite [*Sicardy et al.*, 1999]. Actually, the sizes quoted above are comparable to the Fresnel diffraction scale $L_F \sim \sqrt{\lambda D/2}$, where λ is the wavelength of observation and $D \sim 1.25 \times 10^9$ km is

the distance to Titan, so that L_F varies from 0.8 to 1.6 km when λ varies from 0.5 to 2.2 μm.

[16] Thus the spatial resolution obtained in Titan's atmosphere with these two occultations is close to diffraction-limited, and reaches subkilometer values for both events. Note finally that these stellar diameters are small compared to the typical scale height at the altitudes probed here, $H \sim 50$ km. This allows us to detect fine-scale structures in Titan's stratosphere, as shown in section 5.

[17] Photometric calibrations, where the flux from Titan and the occulted star were measured separately before or after the occultation, were performed at some stations. This allows us to estimate Titan's contribution in the occultation light curves. For instance, in the visible domain, the first star was about as bright as Titan, so that the latter contributes to about 50% of the total flux recorded during the first occultation. Once Titan's flux is subtracted, the normalized stellar flux can be used for analysis, where zero corresponds to total disappearance of the star, and unity corresponds to the full unocculted stellar flux.

[18] The zero stellar flux level is shown as a solid line in Figure 4 for those stations where calibrations were made. Typical accuracy is 1% for the SAAO observations, and a few percent for the other stations. When no photometric
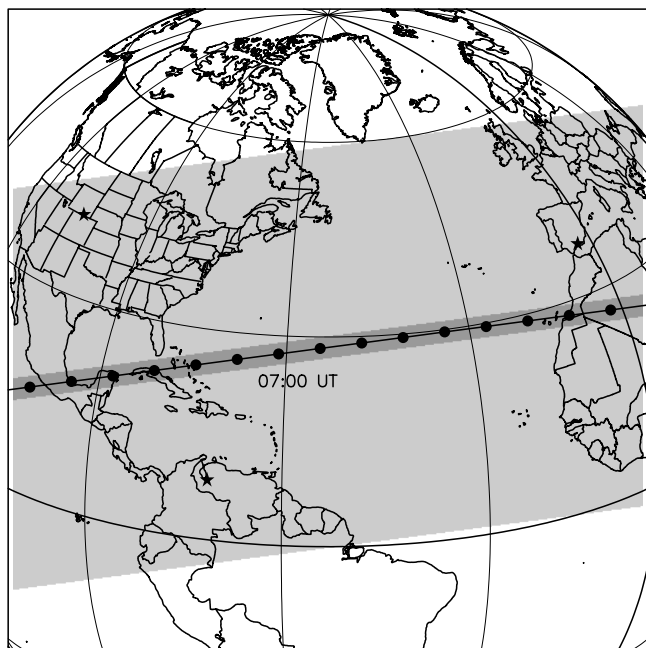
Figure 3. Same as Figure 1, but for the second occultation, except that the size of the map is now 10,000 × 10,000 km. The three observing sites used here are shown as stars symbols in Spain, United States (Wyoming), and Venezuela.

calibrations were available at a given station, only estimations of the zero stellar flux are possible, using other experiments, and are shown as dotted lines in Figure 4.

3. Astrometry

[19] The astrometric reconstruction of the events requires (1) accurate positions for the stars, (2) the ephemeris of Titan and (3) the timing of the occultations. The timing allows us to reconstruct the geometry of the occultation, and provides the offset to apply to Titan's ephemeris, as long as the uncertainties on the star positions remain smaller than this offset.

3.1. Star Positions

[20] The Tycho ICRS position at epoch J2000 for star TYC 1343-1615-1 was taken from the Vizier site. Taking into account the proper motion of the star between J2000 and 14 November 2003, as given in the Tycho catalog, we obtain the following ICRS position at epoch for the first star:

$$\begin{cases} \alpha_1 = 06^h\ 55^{mn}\ 20.9672^s & \pm 0.009\ \text{arcsec} \\ \delta_1 = +22°\ 06'\ 07.812'' & \pm 0.012\ \text{arcsec}, \end{cases} \quad (1)$$

where the error bars in $\alpha \cdot \cos(\delta)$ and δ take into account the uncertainty on the J2000 position, combined with the uncertainty on proper motion. No annual parallax correction has been applied to this position, as it is smaller than the error bars above.

[21] For the second star, TYC 1343-1865-1, the UCAC2 catalog provides the proper motion with better accuracy than the Tycho catalog, with resulting position at epoch (J. Manek, private communication, 2003):

$$\begin{cases} \alpha_2 = 06^h\ 55^{mn}\ 17.7690^s & \pm 0.018\ \text{arcsec} \\ \delta_2 = +22°\ 06'\ 01.226'' & \pm 0.018\ \text{arcsec}, \end{cases} \quad (2)$$

where again no annual parallax correction has been applied.

3.2. Titan Ephemeris

[22] Titan ICRS astrometric position was taken from the online ephemeris of IMCCE (Institut de Mécanique Céleste et de Calcul des Ephémérides) http://portail.imcce.fr/page.php?nav=fr/ephemerides/index.php). This site used the DE405 ephemeris for Saturn, and the TASS 7.1 theory for Titan motion [*Vienne and Duriez*, 1995].

[23] This ephemeris also provides the latitude of sub-Earth point during the occultations, $B = 24°.5$ S, as well as the longitude of sub-Earth point, 238°.8 (the origin of longitudes being the Titan meridian facing Saturn). Titan's north pole position angle is −6°.34 with respect to the J2000 celestial north direction. The resulting aspect of Titan in the sky is shown in Figure 6. The angles given above allow us to calculate the latitudes of the suboccultation points at any moment, as the various stellar images scan Titan's limb; see for instance Figure 10. Note that because the titanocentric elevation of the observer is $B = 24°.5$S, the occultation could probe latitudes between 65°.5S and 65°.5N on Titan. In particular, no information on the polar regions of Titan could be obtained during these occultations. Finally, the distance to Titan was $\Delta = 1.254 \times 10^9$ km for the two occultations, resulting in a scale of 6078 km projected at Titan, per arcsec on the sky.

3.3. Reconstruction of the Occultation Geometries

[24] In order to reconstruct the geometry of the occultation, we need to know at any moment the position of the star relative to Titan's center, projected in the sky plane. We denote by (f, g) the coordinates, in kilometers, of the star in this plane. The origin is taken on Titan's expected center, and the coordinate f is counted positively eastward, while g is counted positively northward. Because of refraction, a ray passing at (f, g) in the plane of the sky will be deviated toward a point with different coordinates (f', g') in the shadow plane.

[25] Because of errors in Titan's ephemerides and on the star position, Titan's actual center is offset with respect to the origin $f' = g' = 0$. To determine this center, we have to use some benchmarks in Titan's atmosphere, which leave their imprint in the observed light curves. Note that the solid surface of the satellite cannot be used since it is not detected during ground-based stellar occultations. Possible benchmarks are the half-light points, where the stellar intensity has been divided by a factor two with respect to its full unocculted value. These points are obtained by fitting isothermal synthetic light curves (the so-called Baum and Code solutions) to the observed light curves. As discussed by *Sicardy et al.* [1999], however, the error bars on those half light points is a fraction of the scale height H, typically ±10 km in the very best conditions, with $H \sim 50$ km. This error is due to the presence of spikes in the light curves,
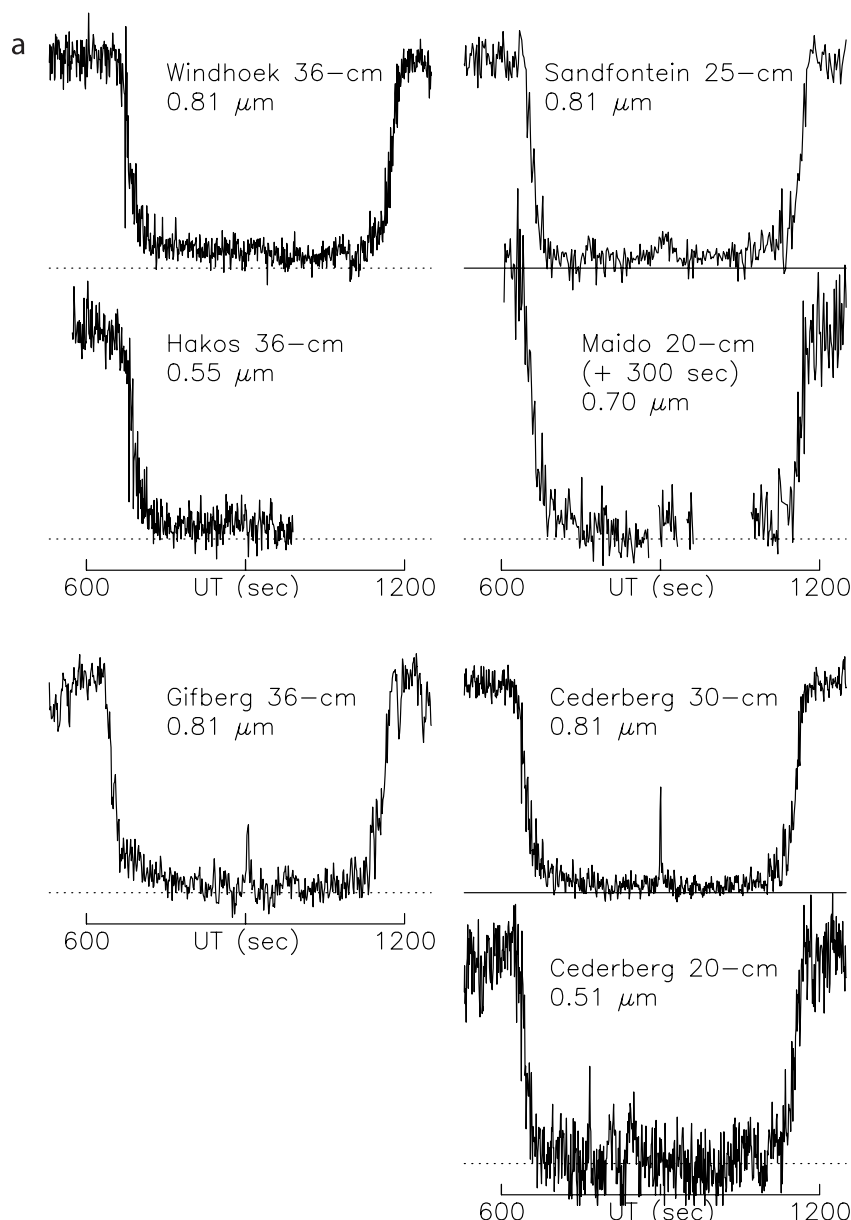
Figure 4. (a) Light curves obtained at various stations during the first occultation. All the data are plotted with a 1-s time sampling, except for the poorer SNR data obtained at Sandfontein and Maïdo, which are plotted with a 2-s sampling. The straight lines (solid or dotted) at the bottom of the occultation light curves mark the zero stellar flux. Solid lines correspond to actual measurements made before or after the occultation; dotted lines are estimations only, in the absence of proper photometric calibration. All the light curves are plotted at the same vertical scale between zero stellar flux and unocculted flux. Note that 300 s have been added to the Maïdo timing to fit into the figure. (b) All the light curves are again plotted at 1-s time resolution. (left) Light curves obtained at Sutherland during the first occultation. (right) Light curves obtained during the second occultation. Note the change in the time axis. The strong fluctuations observed during the occultation at WIRO are due to scattered light from clouds illuminated by the Moon and are not connected with any central flash phenomenon caused by Titan's atmosphere.

errors in photometric calibrations and/or low frequency sky transparency fluctuations.

[26] As noted by *Sicardy et al.* [1999], a better defined benchmark could be used in the 28 Sgr occultation light curves of July 1989. It consisted in a sharp drop of signal followed by a strong spike, caused by a localized inversion layer dubbed "layer A," where the temperature suddenly increases by several Kelvins in a few kilometers. (Another layer "B" was detected in 1989, but with less contrast). All the points corresponding to layer A were found to lie on a common circle, with a typical dispersion of 2.5 km, and the center of this circle was identified to Titan's shadow center.
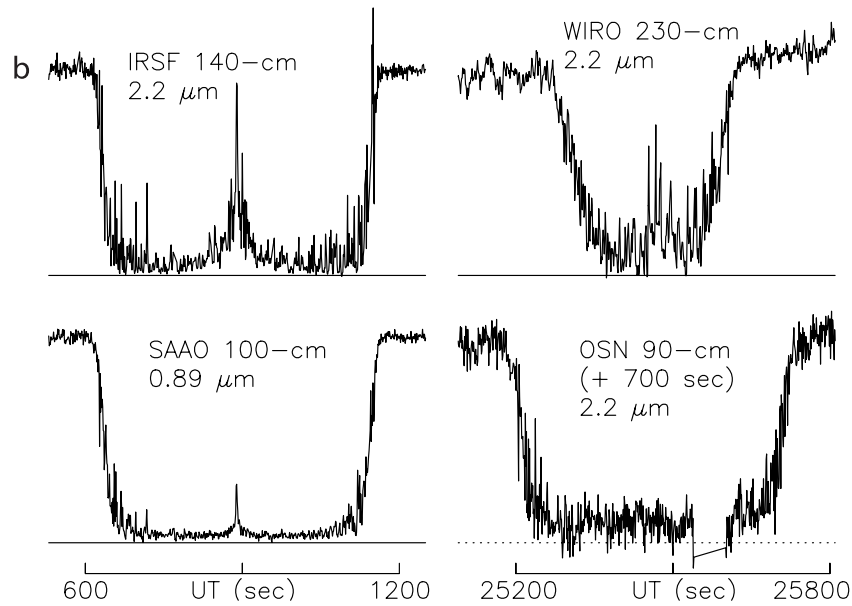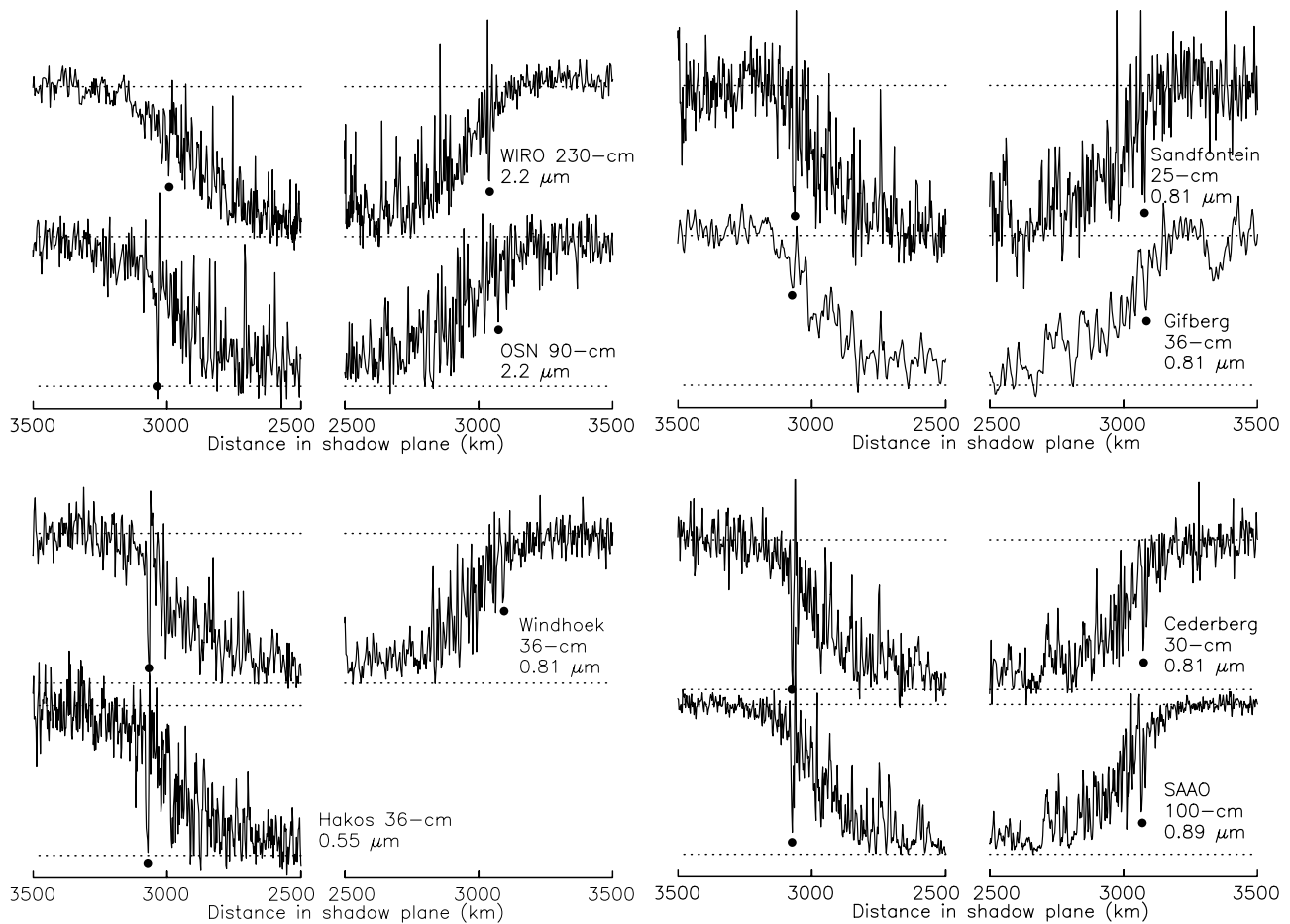
Figure 4. (continued)

Figure 5. Occultation light curves obtained at selected stations. Contrarily to Figure 4, the flux is now plotted at full resolution (as indicated in Table 1). Also, the flux is plotted versus the distance to the shadow center, as defined by equation (3), and not versus time. The dots indicate the location of the dip associated with the inversion layer. Just interior to that dip, a spike is observed and has been used as a benchmark to define Titan's shadow center. The timing of these spikes and corresponding locations in the shadow plane are given in Table 2.

Table 1. Circumstances of Observations

Site (Acronym)	Longitude Latitude Altitude, m	Telescope Aperture, m, Filter	Cycle Time, s	Remarks
First Occultation, La Réunion Island				
La Fournaise (FOU)	55°38′56″E 21°13′53″S 2350	0.265 0.265	– –	clouded out
Les Makes, (MAKE)	55°24′35″E 21°11′57″S 976	0.35	–	clouded out
Maïdo (MAI)	55°23′15″E 21°04′16″S 2205	0.2 (0.7 μm) 0.3	0.4 –	data, partly cloudy technical failure
First Occultation, Republic of South Africa				
South African Astronomical Obs., Sutherland (SAAO)	20°48′38.5″E 32°22′46.0″S 1760	1.0, I (0.89 μm)	0.1	data
Infra Red Survey Facility, Sutherland (IRSF)	20°48′37.7″E 32°22′48.0″S 1760	1.4, K_s (2.15 μm)	1[a]	data
Cederberg (CED)	19°15′09.6″E 32°29′ 58.4″ S 873	0.3, RG715 (0.81 μm) 0.2, BG39 (0.51 μm)	0.27 0.20	data data
Gifberg (GIF)	18°46′59.4″E 31°48′33.5″S 350	0.35, RG715 (0.81 μm) 0.2	0.27 –	data technical failure
Boyden Observatory Bloemfontein (BLO)	26°24′20″E 29°02′20″S 1387	1.52	–	clouded out
Prince Albert (PRI)	22°01′50″E 33°13′56″S 640		–	visual observation
South African Astronomical Obs., Cape Town (CAP)	18°28′38.2″E 33°56′04.5″S 15	0.61	–	clouded out
Nuwerus (NUW)	18°21′28.2″E 31°08′52.5″S 370	0.3 0.2	– –	clouded out
Springbok (SPR)	17°52′58.8″E 29°39′40.2″S 900	0.25 0.20	–	clouded out
First Occultation, Namibia				
Sandfontein (SAN)	18°33′11.1″E 28°42′18.7″S 515	0.25, RG715 (0.81 μm) 0.20	0.22 –	data technical failure
Kleinbegin(KLE)	19°01′27.8″E 27°58′21.0″S 500	0.2	0.2	mostly cloudy
Tivoli (TIV)	18°01′01″E 23°27′40″S 454	0.28, RG715 (0.81 μm)	–	clouded out
Hakos (HAK)	16°21′12″E 23°14′42″S 1834	0.36, broad band (0.55 μm) 0.45	0.2 –	data technical failure
Windhoek (WIN)	17°06′32.0″E 22°41′54.5″S 1920	0.36, RG715 (0.81 μm)	0.33	data
Second Occultation				
Instituto Astronómico de Andalucía, Observatorio de Sierra Nevada, Spain (OSN)	03°23′05″W 37°03′51″N 2896	1.5, I (0.89 μm) 0.9, K (2.2 μm)	– 0.33	too bright sky (sunrise) data
Wyoming Infrared Observatory, USA (WIRO)	105°58′34″W 41°05′50″N 2943	2.3, K (2.2 μm)	0.52	partly cloudy
Observatorio Nacional, de LLano del Hato, Mérida, Venezuela (MER)	70°52′00″W 08°47′00″N 3600	0.65, broad band (0.55 μm)	0.21	very low SNR

[a]Cycle time was 1 s, but exposure was 0.1 s, so that no continuous data set is obtained.
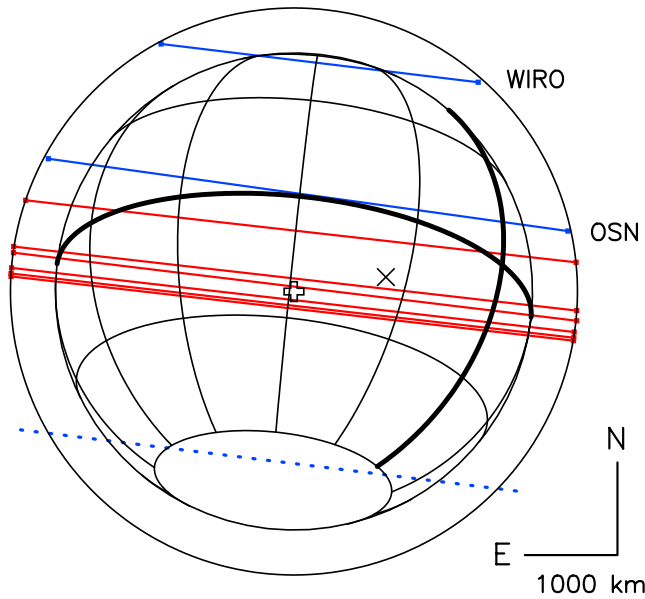
Figure 6. Titan's aspect for the two occultations of 14 November 2003. Celestial J2000 north and east directions and the scale in kilometers are given by the straight segments at the lower right corner. One arcsec corresponds to 6078 km projected at Titan, and the sphere represents the solid surface of a satellite, with a radius of 2575 km. The thick parallel delineates Titan's equator, and the thick meridian represents the anti-Saturn direction (i.e., longitude 180° on Titan). The times symbol (×) gives the expected Titan's center using the DE405 + TASS7.1 Titan ephemeris and the star position of equation (1). This center is the origin of the (f', g') coordinates used in the text. The red lines show the chords observed during the first occultation, using the timings of Table 2. They correspond, from south to north, to SAAO, Cederberg, Gifberg, Maïdo, Sandfontein, and Windhoek (see Figure 7 for an expanded view). The cross marks Titan's center according to a circular fit to the red chords. The Observed-Calculated (O-C) shift between the two centers (times and cross) is 0.163 arcsec toward the east ($\Delta f' = +992$ km) and 0.026 arcsec toward the south ($\Delta g = -155$ km). The blue lines are the chords observed at OSN and WIRO, during the second occultation. They have been shifted to lie on the circle defined by the red chords; see text for details. Finally, the dotted line is the chord observed at Mérida, for which no usable light curve could be derived.

In other words, we assumed that all the detected points of layer A were at the same distance from Titan's center, i.e., at the same altitude above Titan's surface (assuming a spherical satellite). Note from *Sicardy et al.* [1999] that the Titanocentric latitudes of the detected points in layer A spanned the interval 46°S to 20°N, i.e., a good fraction of Titan's limb.

[27] A further validity check of this method was provided by the fact that the center derived from layer A was found at only 3 kilometers away from the center determined by the central flash analysis [*Hubbard et al.*, 1993].

[28] The same method was used here, as a well-defined layer is observed in all the light curves. Again, we will see that the position of Titan's center derived from this layer is consistent with the center derived from the central flash analysis. Table 2 gives the timings of the strong spike associated with the inversion layer, together with the (f', g') coordinates of the observer with respect to Titan's shadow center at that time. The timing errors are taken as the half width at half maximum of the spike associated with the inversion layer. Also provided in Table 2 are the velocities of the various stations in the shadow plane.

[29] In this process, it appeared that the SAAO timing was lagging by 2.7 s when compared to all the other stations. This is true not only for the sharp drops and spikes associated with the inversion layer, but also with the central flash, when compared to the other stations. The timings at the latter stations are mutually consistent, and were directly provided by a GPS associated with the data acquisition chain. A careful check of the time acquisition at SAAO, and of the time broadcast by the South Africa national time service did not reveal any anomalies. Thus we have no explanation for this discrepancy at the time being. Because SAAO is the only station with this problem, we decided to add 2.7 s to the timing at this station in order to be consistent with the other experiments.

[30] The timings for the inversion layer are given in Table 2, and the resulting chords are shown in Figure 6 for both occultations. A circular fit to the limb corresponding to the first occultation chords (i.e., excluding the OSN and WIRO chords in Table 2) provides the radius and center of the circle with best fits the projection of the inversion layer in the shadow plane. The radius is found to be $R_{\mathrm{IL}} = 3060$ km, with a radial dispersion (r.m.s.) of 3.5 km, corresponding to about 0.3 s in time. This dispersion is consistent with the typical timing errors given in Table 2. This means that we cannot detect a significant departure from circularity for the inversion layer in the shadow plane. Note that the radius given here applies to the shadow plane, and consequently, does not take into account the ray bending due to refraction in Titan's atmosphere. The actual radius of the inversion layer at Titan is larger by 30 ± 5 km due to this bending, so that the altitude of the inversion layer is eventually found to be 515 ± 6 km; see section 5 for details.

[31] A by-product of the circular fit is the position of the inversion layer center in the shadow plane. The cross symbol in Figures 6, 7, and 12 represents Titan's center after a circular fit has been performed on the red chords, corresponding to the first occultation only. The discrepancy between the calculated (times symbol) center, where the origin of f' and g' are taken, and the observed (cross symbol) centers stems from a combination of possible errors on Saturn's ephemeris around the Sun, on Titan's ephemeris around Saturn and on the star position.

[32] The O-C offset between these two centers is:

$$\left\{ \begin{array}{l} \delta f' = 992 \pm 4 \ \mathrm{km} \\ \Delta g' = -155 \pm 25 \ \mathrm{km}, \end{array} \right. \qquad (3)$$

The error bars are at 3σ level, assuming that the inversion layer is spherical and concentric with Titan's solid body. The error in g' is larger because the chords for the first occultation are clustered near Titan's diameter; see Figure 6. Actually, most of the constraint on $\Delta g'$ comes from the northernmost Windhoek chord. The center given above

Table 2. Geometry of the Inversion Layer

| Station	Immersion,[a] s UT	Velocity,[b] km s^{-1}	f', km	g', km	Lat,[c] deg	Emersion,[a] s UT	Velocity,[b] km s^{-1}	f', km	g', km	Lat,[c] deg
SAAO[d]	625.6 ± 0.05	11.712	−2024	−686	−3.3	1147.3 ± 0.05	11.710	4046	+008	−3.0
Cederberg	638.6 ± 0.15	11.706	−2029	−653	−2.7	1161.0 ± 0.40	11.704	4046	+039	−2.5
Gifberg	643.3 ± 0.40	11.707	−2033	−592	−1.7	1165.5 ± 0.70	11.705	4041	+100	−1.4
Maïdo	350.7 ± 0.25	11.818	−2060	−470	0.4	0869.4 ± 0.60	11.800	4020	+263	1.4
Sandfontein	650.1 ± 0.15	11.717	−2059	−360	2.3	1172.2 ± 0.20	11.715	4018	+330	2.5
Hakos	678.0 ± 0.15	11.724	−2060	+137	10.7	n.a.	n.a.	n.a.	n.a.	n.a.
Windhoek	674.0 ± 0.15	11.729	−2053	+160	11.1	1183.8 ± 0.15	11.727	3888	+830	11.3
OSN	24506.2 ± 0.15	11.171	−1956	317	17.0	25013.5 ± 0.20	11.151	3652	1098	19.9
WIRO	25294.0 ± 0.70	11.098	−989	1923	48.0	25604.8 ± 0.25	11.098	2436	2337	48.3

[a]On 14 November 2003.
[b]Velocity in the shadow plane.
[c]Titanocentric latitude of suboccultation point.
[d]A correction of +2.7 s is later applied to the SAAO timings provided here when fitting the inversion layer shape, due to a probable clock problem. See text for details.

(equation (3)) is used as a reference point when fitting our central flash model to the data. Some fine adjustments of the shadow center (the parameter $\Delta g''$ in Table 2) are made during that fit; see point 1 in section 6.1 for details.

[33] Using the correspondence 1 arcsec = 6078 km at Titan, the offset given above yields the following offset for Titan in the ICRS system, with respect to the DE405 + TASS7.1 ephemeris:

$$\begin{cases} \delta\alpha \, \cos(\delta) = & 0.163 \pm 0.009 \text{ arcsec} \\ \Delta\delta = & -0.026 \pm 0.012 \text{ arcsec,} \end{cases} \quad (4)$$
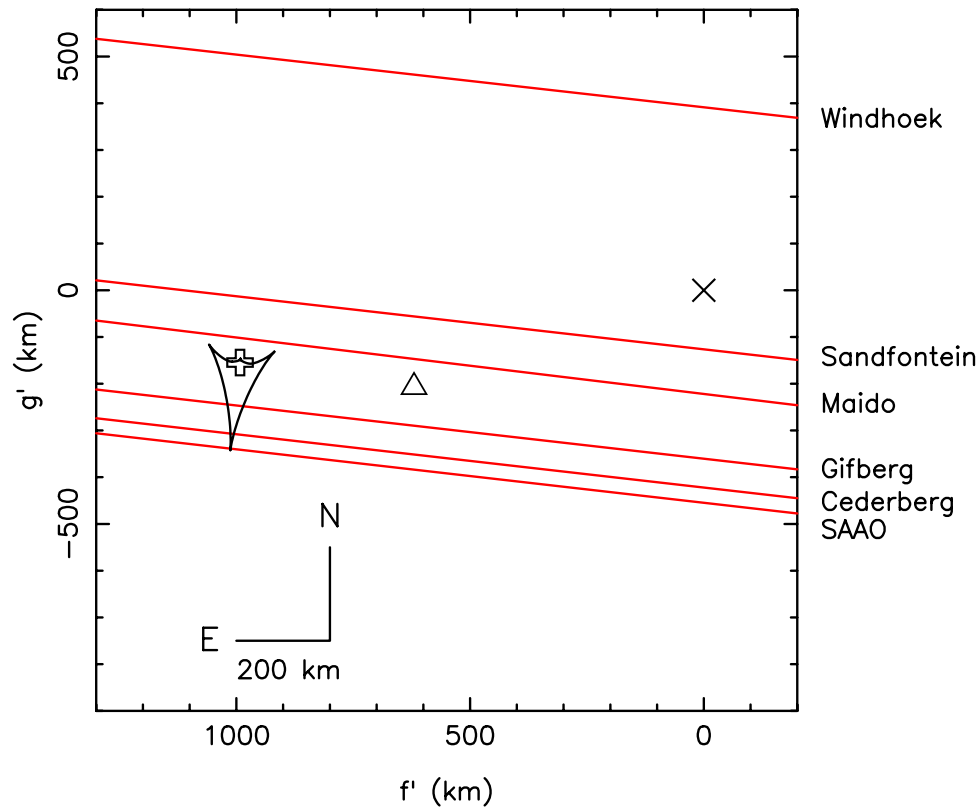
Figure 7. Enlargement of the previous figure showing the central region of Titan. As before, the times symbol is the shadow center expected from the DE405 + TASS7.1 Titan ephemeris, and the open cross is the center of the circular fit to the red chords shown in Figure 6. The spiky, triangular shape near the center of the shadow is the best fit caustics (or evolute) derived from the central flash analysis; see also Figure 12 for a better view of the caustics. Finally, the open triangle is our latest pre-occultation prediction for Titan's center, after we analyzed astrometric fields taken at Observatoire de Haute Provence (France), with both the star and Titan present on the same images.
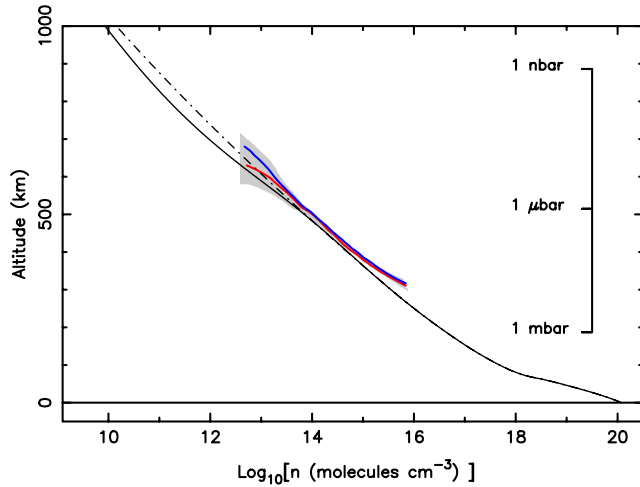
Figure 8. The density profiles $n(z)$ retrieved from the SAAO light curve inversions obtained in I band (0.89 μm). Red curve is for ingress; blue curve is for egress. The gray envelope around the retrieved profiles delimits the overall uncertainty region due to (1) uncertainty in the initial condition at the top of the profiles and (2) the uncertainty in the zero stellar flux level (see the solid or dotted baselines in Figure 4). Errors grow exponentially above 600 km due to the exponential atmospheric decay. Although formal errors at the bottom of the profiles remain small, note that there is a systematic bias due to the presence of absorbing hazes in Titan's atmosphere; see text. The solid curve is the nominal model of *Yelle* [1991], while the dot-dashed profile line comes from a reanalysis by *Vervack et al.* [2004] of the Voyager 1 UVS solar occultation.

where most of the error bars now come from the uncertainty on TYC 1343-1615-1 position.

[34] The second occultation can provide in principle an independent value for this offset. The position of TYC 1343-1865-1, however, is not so accurately determined (equation (2)) as for TYC 1343-1615-1. Moreover, only two chords are available for the second occultation, with light curves of poorer SNR than for the first event. Finally, the WIRO chord is rather far to the north, with probed latitudes reaching 48°N; see Table 2. Thus some (unknown) oblateness effect could alter our determination of Titan's shadow center for these chords. Assuming that the inversion layer is spherical everywhere, then from the second occultation Titan's offset would be:

$$\begin{cases} \Delta\alpha\cos(\delta) = 0.165 \pm 0.018 \text{ arcsec} \\ \Delta\delta = -0.055 \pm 0.018 \text{ arcsec,} \end{cases}$$

fully consistent with equation (4) in right ascension, and marginally consistent only in declination. We do not pursue further this analysis in this paper, and we assume that the extremities of the chords of the second occultation lie on the circle defined by the first occultation, as shown in Figure 6.

4. Light Curve Analysis

[35] As an observer on the Earth enters into Titan's shadow, the stellar flux $F_\star$ first decreases by a factor

$f_{ref} < 1$, due to differential refraction by the essentially transparent atmosphere of the satellite. The refractivity of N_2 (see Appendix A) and the distance of Titan then allow us to probe Titan's atmosphere in the altitude range $\sim$250–600 km ($\sim$250 and $\sim$0.15 μbar, respectively). This corresponds to the upper stratosphere and the lower mesosphere of the satellite. For a spherically symmetric transparent atmosphere, we can use an abelian inversion technique to retrieve the molecular density, temperature and pressure profiles $n(z)$, $T(z)$ and $p(z)$ as a function of altitude z above Titan's surface. Details about this technique are given by *Roques et al.* [1994] and *Sicardy et al.* [1999], and results are presented in the next section.

[36] The stellar drop starts to be detectable at $\sim$600 km, and the atmosphere remains transparent down to about 400 km ($\sim$12 μbar); see Figure 8. For deeper regions, however, the stellar flux is not only refracted, but also absorbed by Titan's hazes, and thus multiplied by a factor $\exp(-\tau)$, where τ is the tangential (along the line of sight) optical depth of the haze layer. At that point, the inversion technique is no longer valid, and the retrieved profiles are no more reliable. However, information on the haze opacities and distribution can be obtained; see section 8.

[37] Finally, as the observer gets close to the shadow center, the stellar flux gets multiplied by a focusing factor $f_{foc} > 1$ due to limb curvature. This factor remains close to unity during ingress and egress, but becomes larger and larger as the shadow center is approached. Consequently, the stellar flux

$$F_\star = f_{ref} \times f_{foc} \times \exp(-\tau) \qquad (5)$$

can increase again, causing the so-called central flash; see section 6. The extreme sensitivity of f_{foc} to limb curvature allows one to retrieve precisely the limb shape.

[38] We thus split our analysis in two parts: the ingress and egress of the star (probing altitudes between 600 and 400 km), where atmospheric profiles can be derived though inversion, and the central part of the occultation (altitudes between 400 and 250 km), where information on aerosol distribution and precise shape of the isopycnals (iso-density levels) can be gathered.

5. Titan's Stratospheric Profiles

[39] The ingress and egress stellar light curves are now used to derive Titan's upper stratosphere profiles. We assume a pure molecular nitrogen atmosphere, and the prime result deduced from these light curves are the molecular density profiles as a function of altitude, $n(z)$, using the so-called inversion technique; see *Roques et al.* [1994] for details. Here, we only use the light curves obtained at SAAO in I band during the first occultation, as it is the highest SNR data set. A detailed comparison with the other data sets obtained during the two occultations will be presented elsewhere.

[40] The main uncertainty in the derived profiles comes from the fact that the SNR ratio become exponentially small as higher altitudes are probed. Practically, above about 600 km ($\sim$0.15 μbar), no useful information on the atmosphere can be extracted. At those altitudes, an initial condition must be given, namely, a given refractivity
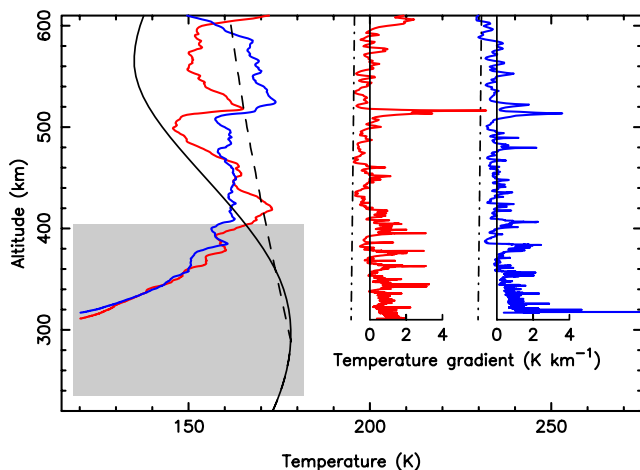
Figure 9. The retrieved temperature profiles obtained from the SAAO light curve (red, ingress; blue, egress). The solid curve is the nominal model of *Yelle* [1991], while the dashed curve is the *Vervack et al.* [2004] profile. The gray area indicates the altitude range where haze absorptions start to influence the retrieved temperature profiles. The two profiles on the right show the corresponding temperature gradient profiles, with the dash-dotted line showing the adiabatic lapse rate beyond which convective instabilities should develop. Note the conspicuous and sharp inversion layer near the 515 ± 6 km altitude level; see the text for details.

(equivalent to a given density, if composition is known) at a given altitude (equivalent to a given time in the light curve). At this time, the occultation is considered to have started, i.e., differential refraction becomes significant compared to the noise caused by the star scintillation in Earth's atmosphere. Using various initial conditions, we obtain a whole family of possible profiles, which converge toward a common profiles below ∼500 km (∼1.4 μbar), see for instance the convergence of the ingress and egress profiles in Figure 8.

[41] Another source of errors comes from absorbing hazes below ∼400 km, where the inversion procedure is no longer valid, as noted before. Practically, the stellar flux is smaller than what it would be without aerosols, which is interpreted as a drop of scale height in the inversion code. This explains the systematic increase of the retrieved profiles from the expected behavior (i.e., *Yelle*'s [1991] model) below $z = 400$ km; see Figure 8. Below ∼300 km, no useful information can be gathered in terms of density profile. As layers deeper than ∼250 km are probed, however, we start to detect the so-called central flash, whose analysis is presented in next section.

[42] The aerosol problem is evident in Figure 9, where the temperature is apparently found to steadily decrease below 400 km, an artifact due to light absorption as explained above. Turning the problem around, we can use the recent Huygens/HASI descent temperature profile [*Fulchignoni et al.*, 2005] to deduce the aerosol opacity profile at those altitudes, assuming that the SAAO temperature profiles obtained in November 2003 at 3°S are the same as the HASI profile obtained in January 2005 at 10°S. This work is out of the scope of the present paper, and will be presented elsewhere.

[43] It is important to point out here that the temperature profiles $T(z)$ shown in Figure 9 depend on arbitrary initial

conditions T_0 at given altitudes z_0. This is a well-known problem in inversion techniques, discussed, for instance, by *Roques et al.* [1994] and *Elliot et al.* [2003]. The initial conditions in Figure 9 have been chosen so that our profiles are roughly isothermal in the upper part of the diagram. Other profiles are possible, however, so that we cannot dismiss *Yelle*'s [1991] temperature profile, since other initial conditions could have been chosen to match the general mesospheric decrease predicted by this author.

[44] Several noteworthy features are visible in Figures 8 and 9:

[45] 1. There is a good agreement between our density profiles and *Yelle* [1991] predictions in the 400–500 km altitude range. However, a closer inspection shows that our density profiles are about 35% denser (at a given altitude) than *Yelle*'s [1991] profile in that altitude range (or about 15 km higher, for a given density). Considering our uncertainty domain, this discrepancy remains nevertheless marginal. A detailed comparison with the Huygens profile should confirm or dismiss that point.

[46] 2. Our observations cannot distinguish between *Yelle*'s [1991] and *Vervack et al.*'s [2004] models because our error bars become too large at the altitudes where these two profiles diverge.

[47] 3. The inversion layer already discussed in section 3.3 is conspicuous in Figure 9. Its radius, 3060 ± 3.5 km, should place it 485 km above Titan's surface, if we adopt the classical radius $R_T = 2575$ km for Titan [*Lindal et al.* 1983]. However, ray bending due to refraction in Titan's atmosphere during the occultation amounts to about 30 ± 5 km at the level of that layer, where the error bar comes from uncertainties in the initial conditions used during the inversion procedure (namely, the time at which the inversion is started, and the assumed value of density at the corresponding level). The inversion layer is then found at 515 ± 6 km (∼1.5 μbar pressure level).

[48] At that level, the temperature locally increases by 15 K in only 6 km, and the peak value of the gradient dT/dz reaches values as high as $+6$ K km^{-1} at ingress (Figure 9). Note that the temperature gradient is always bounded, on the negative side, by the adiabatic lapse rate $\Gamma = -g/c_p$, where g is the acceleration of the gravity and c_p is the specific heat at constant pressure. Taking $c_p = 1.04 \times 10^7$ erg K^{-1} g^{-1} for molecular nitrogen and $g = 101.4$ cm s^{-2} at 400 km, we get $\Gamma \sim -1$ K km^{-1} in the region of interest.

[49] The inversion layer near 515 km has actually been confirmed by the in situ measurements of the Huygens Atmospheric Structure Instrument (HASI) during the entry of the probe in Titan's atmosphere on 14 January 2005 [*Fulchignoni et al.*, 2005]. The HASI inversion layer is found around 507 ± 15 km, i.e., about 8 km lower than the layer we observe in November 2003. The ± 15 km error bar stems for uncertainties in the initial probe velocity vector at entrance in Titan's atmosphere, so that the discrepancy between the two altitudes for the inversion layer is not confirmed at this point. A detailed comparison of our observations and HASI profile will be presented in Paper 2. The stability of this layer both in space (from at least 3.3°S to 11.3°N in November 2003; see Table 2) and time (from November 2003 to January 2005) is obviously remarkable for such a vertically localized and sharp feature.

[50] Note finally that the 28 Sgr occultation on 3 July 1989 did show the existence of two conspicuous inversion layers, one at 425 km (~7 μbar), the so-called "layer A" of *Sicardy et al.* [1999], and one at 450-455 km (~4 μbar), or "layer B." These layers were thus respectively 90 and 60 km deeper than the layer shown here, i.e., more than one scale height H deeper, with H~50 km around 500 km.

6. Central Flash Analysis

[51] The increase of stellar signal near the center of the shadow is caused by the focusing of rays by Titan's limb; see equation (5).

[52] In principle, and once the refractive properties of the atmosphere have been defined (composition and density profile), the shape and intensity of this central flash provide the (1) shape of the layer causing the flash and (2) the tangential (along the line of sight) optical depth of the regions scanned by the stellar images. If several wavelengths are used, as it is the case here, we also get (3) the wavelength dependence of this optical depth.

[53] In practice, modeling the central flash is a challenging and arduous task, as we only have a finite number of cuts across the flash region (see Figure 12), and not a full 2-D map of the flash itself. More importantly, reproducing the central flash relies on a large number of free parameters, in order to define the shape and optical depth of the layer responsible for the flash at all latitudes ϕ. In principle, we should specify the properties of this layer down to a resolution of a few kilometers, corresponding to the stellar diameter projected at Titan.

[54] Considering the noise level in the light curves, we have to simplify our model in order to reduce this large number of free parameters to a tractable number. The critical quantities here are the limb shape, which provides the factor f_{foc} in equation (5), and the aerosol distribution, which provides the optical depth $\tau(z, \phi)$ at altitude z and latitude ϕ. The refraction factor f_{ref} in equation (5) is less critical as it is robustly provided by current Titan atmospheric models, as pointed out in Appendix A. The parameters associated with these quantities are now examined.

6.1. Parameters of the Fits

[55] We explain in Appendix A how the factors f_{ref}, f_{foc} and $\tau(z, \phi)$ are derived, so that a central flash can be generated along any given trajectory in the shadow. The aim is to adjust the shape of the central flash layer to best fit the observations. Once this shape is found, it is possible to derive the Titan zonal wind regime, by assuming that the isobar levels are in equilibrium under the combined effects of Titan's gravity and the centrifugal acceleration field associated with the zonal winds. We neglect for the moment pressure gradients caused by meridional temperature gradients. Thus the isobar levels also correspond for the moment to isopycnic (constant density) levels, The so-called barotropic approximation. This approximation was also used in the 1989 Titan central flash analysis [see *Hubbard et al.*, 1993], and it is discussed again in section 7.

[56] The free parameters of this model are as follows:

[57] 1. The location of Titan's shadow center. The astrometric reconstruction described in section 3 is accurate to within ~25 km in the N-S direction (equation (3)). This is not enough to satisfactorily describe the path of the various observers in the central flash region. Actually, a change of a few kilometers in the N-S direction is enough to change significantly the shape of the flashes. Note, however, that the main uncertainty on the shadow center position is in the N-S direction, due to the essentially diametral and E-W orientation of the occultation chords (Figure 6). Actually, the sharp aspect of the flash strongly constrains its timing and leaves little freedom for the shadow center position in the E-W direction. Thus only one free parameter is to be adjusted here, namely, an extra N-S shift $\Delta g''$ to be applied to Titan's center. A positive value for $\Delta g''$ means that we move Titan's center northward in the sky, on top of the offset given in equation (3).

[58] 2. The shape of the central flash limb. The shape of the isopycnic limb causing the flash determines the shape of the evolute of that limb (or caustics), i.e., the centers of curvature where the stellar rays converge, see Figure 12 and Appendix A. Unfortunately, defining that limb requires a large number of free parameters as commented above. To overcome this difficulty, a possibility is to expand the limb shape in a finite number of Legendre polynomials, and then invert that shape to obtain the zonal wind profile. This is what we did for modeling the 1989 central flash [*Hubbard et al.*, 1993], but this approach creates spurious high frequency oscillations in the limb shape, translating into spurious zonal wind fluctuations versus latitude.

[59] We use here an opposite, forward modeling procedure. Namely, we start from a zonal wind regime at the level of the central flash layer (about 250 km altitude at the equator, corresponding to 0.25 mbar). From this wind regime we deduce the shape of the central flash layer, and then the shape of the central flashes through the ray tracing procedure presented in Appendix A. We use the same procedure as already followed by *Hubbard et al.* [1993]. Namely, we first assume that the isopycnic central flash layer coincides with an isobar (the barotropic approximation), i.e., that the temperature is constant along that layer. This assumption is discussed quantitatively in section 7, as meridional temperature contrasts are actually observed at those altitude levels.

[60] We derive the shape of an isobar by posing the hydrostatic equilibrium under the effect of gravity and centrifugal acceleration:

$$\nabla p = -\rho\{\mathbf{g} - [v^2(r, \phi)/r_\perp] \cdot \mathbf{u}_\perp\}, \qquad (6)$$

where p is the pressure, ρ is the mass density, $r_\perp$ is the distance to Titan's spin axis, $\mathbf{u}_\perp$ is the unit radial vector perpendicular to Titan's spin axis, and $v(r, \phi)$ is the zonal wind velocity at distance r from Titan's center and at latitude ϕ. Finally, $\mathbf{g}$ is the acceleration of gravity, assuming that Titan is spherically symmetric with $GM_T = 8978.2$ km^3 s^{-2}, where G is the gravitational constant and M_T is Titan's mass. One can obtain the shape $r(\phi)$ of the isobar by using equation (6), which states that the isobaric surface is always perpendicular to the vector $\mathbf{g} - [v^2(r, \phi)/r_\perp] \cdot \mathbf{u}_\perp$. This yields the following differential equation:

$$\frac{r'}{r} = -\frac{f \cos\phi \sin\phi}{1 - f \cos^2\phi}, \qquad (7)$$

where $r' = dr/d\phi$ and $f \ll 1$ is the rotation parameter, $f(r, \phi) = r^3\omega^2/GM_T = rv^2/(GM_T \cos^2\phi)$. When integrating this equation, we assume that the wind profile $v(r, \phi)$ is locally independent of r, a reasonable assumption since the layer causing the central flash is very thin (Appendix A). Note that equation (7) can be inverted, yielding the zonal wind velocity v, once the shape $r(\phi)$ of a isobaric level is given:

$$v^2 = -g\cos(\phi)\frac{r \cdot r'}{r\sin(\theta) - r'\cos(\theta)}. \qquad (8)$$

[61] Our problem is now to find a function $v(\phi)$ which is simple enough to be implemented in our numerical procedure, but still complex enough to capture the main characteristics of Titan's wind regime at those altitudes. As it turns out, however, a robust result of our observations is that the distribution of light in the central part of the shadow exhibits a strong asymmetry in the north-south direction. A station like Sandfontein, which is roughly symmetric to Gifberg with respect to the shadow center (Figure 12) provides a very different central flash profile (Figure 11). Another robust result is that the the evolute in the central flash region is an elongated triangular pattern pointing toward the south and parallel to Titan's rotation axis (Figure 12), instead of an equilateral diamond shape expected for a simple ellipsoidal figure for the limb. This confirms and completes the results derived from the 28 Sgr occultation in 1989 [Hubbard et al., 1993], and shows that the wind regime has a strong north-south asymmetry, with stronger jets in the northern latitudes. The difference with 1989, however, is that the shape of the evolute is reversed along the north-south direction. This is expected as half a Titanian year or so has elapsed between 1989 and 2003, so that the two hemispheres must have swapped their wind regime between the two dates.

[62] Thus, to reduce further the number of free parameters, we chose to use the Titan General Circulation Model (GCM) derived by Rannou et al. [2004]. This model provides, among other things, the zonal wind regime at various altitudes, from which we extract the wind profile $v(\phi)$ at 250 km altitude. We then investigate whether a modified profile

$$v'(\theta) = \eta \times v(\theta) \qquad (9)$$

can satisfactorily reproduce our observations, where η is an ad hoc constant scaling factor. This leaves us with only one free parameter, η, for describing the wind regime.

[63] Admittedly, this reduces the wind regime to one particular family. However, this prescription is justified if it allows us to simultaneously capture the gross characteristics of the five central flashes observed during the occultation (Figure 11). This will indicate that Rannou et al.'s [2004] wind profile captures the main characteristics of that circulation, namely, a strong northern jet versus a weak wind regime in the southern hemisphere. Of course, we cannot exclude that other solutions are possible. This point is discussed later on.

[64] 3. The aerosol distribution, which provides the tangential (along the line of sight) optical depth for the

various stellar images (near and far-limb) moving along the limb during the occultation. The trajectories of these images are displayed in Figure 10. Again, a large number of parameters would be necessary to describe this distribution. To overcome this difficulty, we adopt a very simple aerosol distribution; see below and Figure 14.

[65] During immersion and emersion, the stellar images follow essentially vertical trajectories near the equator, first traversing the so-called detached haze layer around 500 km and then probing larger and larger optical depths; see upper panel of Figure 14. After this phase, when the images reach altitudes lower than $\sim$245 km, they move along essentially horizontal trajectories, in the so-called main haze layer. We will see that two main regions are encountered at those altitudes: more opaque regions in the southern hemisphere up to mid-northern hemisphere ($\tau \sim 2$ in the I band) and less opaque regions near the north pole (where $\tau \sim 1$).

[66] Thus, for altitudes $z \leq 245$ km, the tangential optical depth τ is assumed to be constant with altitude, but not with latitude. More precisely, we take $\tau = \tau_{\text{sup}}$ for latitudes $\phi \geq \phi_{\text{sup}}$, and $\tau = \tau_{\text{inf}}$ for latitudes $\phi \leq \phi_{\text{inf}}$, with $\phi_{\text{inf}} < \phi_{\text{sup}}$. Between ϕ_{sup} and ϕ_{inf}, the variation of τ is assumed to be linear versus ϕ, with the boundary values of τ_{sup} and τ_{inf} at ϕ_{sup} and ϕ_{inf}, respectively. For altitudes $z > 245$ km, we assume an exponential dependence $\tau(z) = \tau(245 \text{ km}) \cdot \exp[-(z - 245)/H_\tau]$. The free parameters describing the aerosol distribution are thus the optical depths τ_{sup} and τ_{inf}, the bounding latitudes ϕ_{sup} and ϕ_{inf}, and the scale height H_τ.

[67] As we will see, the transition between τ_{sup} and τ_{inf} occurs in a rather narrow latitude interval, typically between 40°N and 55°N; see Table 3. Thus τ_{sup} represents tangential optical depths in northern regions (ϕ from $\sim$55°N to 65°.5N), while τ_{inf} is typical of mid-northern latitudes and the entire south hemisphere, down to 65°.5S.

[68] 4. The smoothing parameter for the light curves. All our attempts to model the light curves clearly show that the calculated central flashes are too narrow and spiky compared to the observations. Even taking into account the effect of the stellar diameter projected at Titan (about 2.2 km; see section 2) and the Fresnel diffraction scale (about 2 km as well), the calculated central flashes remain too sharp. We thus apply some extra smoothing, parameterized by an equivalent stellar diameter D_{sm}, which turns out to be more than ten times larger than the actual stellar diameter, as discussed below.

[69] 5. The optical depth wavelength dependence. All the optical depths quoted in the text are for the I band (0.89 μm). Now, the Sutherland station provides two lightcurves, one in the I band (SAAO, 0.89 μm) and the other one in the K_s band (IRSF, 2.2 μm); see Table 1. Similarly, the Cederberg station provides two light curves, one in the visible (0.51 μm) and one in the red (0.81 μm). Because the observations are made at the same place, the difference in the central flashes (see Figure 15) is solely due to the chromatic dependence of $\tau(\lambda)$. As done by Hubbard et al. [1993], we assume that this dependence is given by $\tau \propto \lambda^{-q}$, where q is a free parameter to be adjusted to fit the observations. Thus the optical depths at any wavelength is obtained by $\tau(\lambda) = \tau(0.89 \ \mu\text{m}) \times (0.89/\lambda_{\mu\text{m}})^q$.

[70] Note in passing that the data obtained at Cederberg, Gifberg and Sandfontein have an equivalent wavelength of
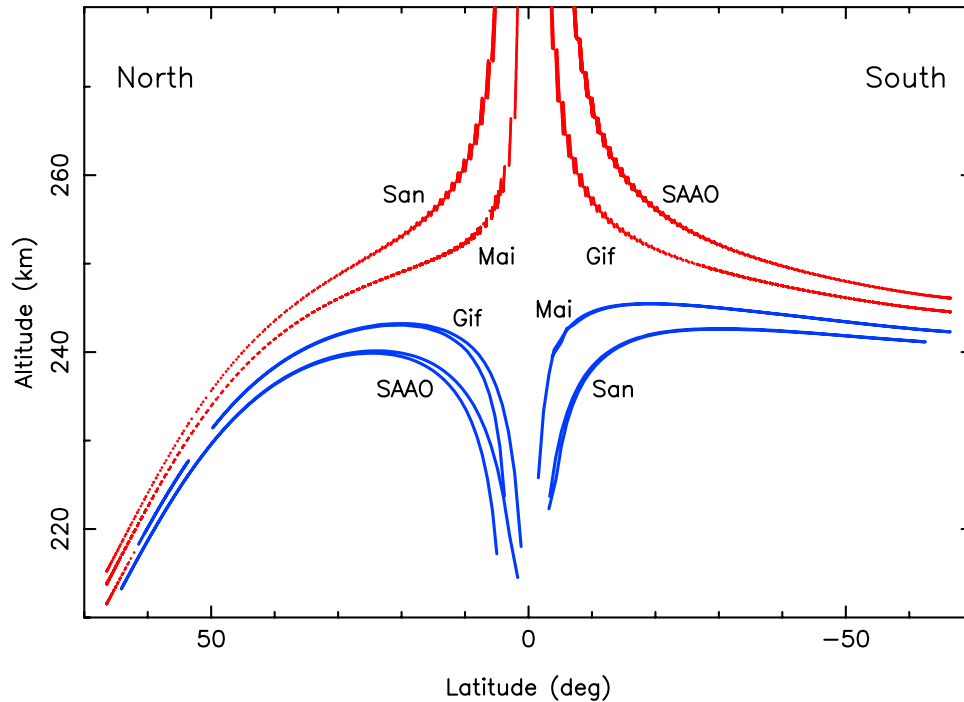
Figure 10. The trajectories of the near-limb (red) and far-limb (blue) stellar images in Titan's atmosphere, for the stations where a central flash was observed. (The Cederberg and IRSF trajectories are not plotted for clarity, however, because they lie very close to the SAAO trajectories). For this figure, we have taken a value of $\eta = 1.10$, which gives winds 10% larger than those of *Rannou et al.* [2004]; see equation (9). See also Table 1 for the meaning of the acronyms.

0.81 μm (Table 1), too close to SAAO (0.89 μm) to usefully constrain the value of q.

[71] The procedure describes in Appendix B is then applied to find the best fit of the model to the data and derive the relevant physical parameters we are interested in, namely, the zonal wind profile, the haze distribution and the haze opacity wavelength dependence.

6.2. Fit to the Observed Central Flashes

[72] We have explored values of η which remain consistent with the astrometric solution given in section 3.3, namely, values which keeps the N-S extra shift of Titan's center, $\Delta g''$, to within ± 25 km. This is achieved for $1.02 \leq \eta \leq 1.15$; see Table 3. As discussed below, values of η higher than 1.15 are furthermore rejected because they predict too strong a flash at the Maïdo station. Also, values of η lower than ~ 1 predict too strong a flash at Gifberg. Table 3 provides the parameters corresponding to our best fits with $1.02 \leq \eta \leq 1.15$. Typical errors for τ are ± 0.1, due to noise in the data and errors in the photometric calibrations. Note that all the fits use a smoothing disk of diameter $D_{\text{sm}} = 24.6$ km in the shadow plane. This is one order of magnitude larger than the stellar diameter projected at Titan (2.2 km; see section 2).

[73] This means that unmodeled smoothing processes are at work in the flash formation. This could be due to localized inhomogeneities in Titan's atmosphere, caused by gravity waves, which could blur the caustics in the central flash region. We note that a similar problem was encountered during a stellar occultation by Neptune in

1985, during which a central flash was observed. The latter was affected by broad spikes, possibly caused by extended barlike patterns lying parallel to Neptune's limb [*Hubbard et al.*, 1988], a typical signature of gravity waves. As explained by *Narayan and Hubbard* [1988], it is not really appropriate then to apply a ray-tracing analysis to this part of the lightcurves. Actually, in this strong scintillation regime, multipath trajectories appear for the photons, so that the notion of single ray is lost.

[74] An illustration of the effect of scintillation in the flash region is possible, however, and is provided in Figures A2, A3, and A4. In this model, we perturb the isopyc central flash layer so that its altitude varies by typically ± 300 m over horizontal wavelengths randomly chosen between 170 and 1050 km, see Appendix A for details. These amplitudes and wavelength range were chosen so that to match the spread observed in the central flashes; see for instance Figure A4. It remains to be seen how these small perturbations of the isopyc layer can be caused by propagating gravity waves. However, the vertical

Table 3. Parameters of the Central Flash Best Fits

η	$\Delta g''$, km	τ_{inf}[a]	τ_{sup}[a]	H_τ, km	ϕ_{inf}, deg	ϕ_{sup}, deg	q	$D_\star$, km
1.02	−23.0	2.2	1.15	40	40N	55N	1.5	24.6
1.10	+5.0	2.2	1.10	40	40N	55N	1.7	24.6
1.15	+24.0	2.2	1.05	40	40N	55N	2.0	24.6

[a]At 0.89 μm.
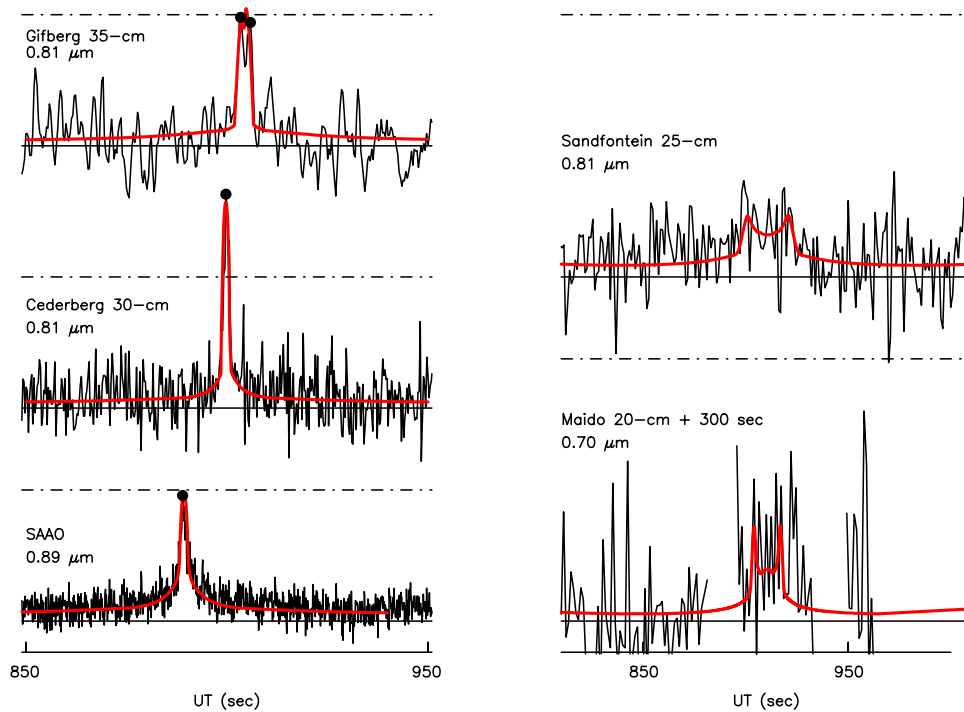
Figure 11. Best fits to the central flashes obtained between 0.70 and 0.89 μm, using a value $\eta = 1.10$, i.e., zonal winds 10% more intense that those of *Rannou et al.* [2004]. The haze opacities given in Table 3 have also been applied. Finally, all the theoretical profiles have been smoothed with a smoothing parameter of $D_{sm} = 24.6$ km; see Appendix A. All the light curves in the left panel have been plotted at full resolution (see Table 1), while the noisier data in the right panel have been smoothed to a resolution of 1.2 s and 0.90 s for Maïdo and Sandfontein, respectively. The bullets in the left panels indicate for clarity where the maxima of the flashes are reached. The horizontal solid line indicates the zero stellar flux, while the dash-dotted line marks the 40% of the unocculted stellar flux. Note the compression by a factor two in the timescale of the right panel with respect to the left panel, and the expansion by a factor two in the vertical scale, to enhance the flash visibility. Note finally that 300 s have been added to the Maïdo timing in order to align the central flash with Sandfontein.

amplitudes quoted above (a few hundred meters) represents typically 1% or less of the scale height at that level, a reasonable fraction at that altitude ($\sim$250 km) as already discussed by *Sicardy et al.* [1999]. Similarly, the horizontal wavelengths involved (a few hundreds of kilometers) are those which were typically observed during the 28 Sgr occultation [see *Sicardy et al.*, 1999, Figure 25].

[75] Because ray tracing in the presence of scintillation is time consuming, and because scintillation is a process which conserves the total amount of light, we have decided to apply a simple smoothing with an equivalent stellar diameter of $D_{sm} = 24.6$ km, which satisfactorily reproduce the observed flashes. Thus the quantity D_{sm} is a parameter which globally describes the effect of scintillation in the central flash region. The interpretation of its value in terms of gravity waves near the 250 km altitude level (0.25 mbar) is left for a further study, where a detailed comparison of the various light curves and also a comparison with the Huygens profile will be made.

[76] Satisfactory fits of our model to the data are obtained for η inside the interval 1.02–1.15. The best fit we have obtained is for $\eta = 1.10$, and is shown in Figure 11. Figure 12 shows the intensity distribution in the shadow plane for this

case, together with the trajectories of the various stations in this plane. The best fits obtained for the extreme values $\eta = 1.02$ and $\eta = 1.15$ are shown in Figures B1 and B2. They show some subtle differences with respect to the $\eta = 1.10$ case. For instance the Cederberg predicted flash is a little bit too low, and the Maïdo predicted flash is too high for $\eta = 1.15$, so that the $\eta = 1.10$ value is our preferred one. However, considering the noise in the light curves and the uncertainty in the zero stellar flux baselines, these differences should not be taken as significant.

[77] We have explored lower values of η, for instance $\eta = 0.95$, but then the calculated central flash at Gifberg becomes too high when compared to the observations. At the upper end of the interval ($\eta = 1.15$), the Maïdo station should cross the caustics, yielding too strong a flash; see Figure B2. It thus appears that the constraints provided by the astrometry are consistent with the constraints provided by the shapes of the flashes.

7. Zonal Wind Profile

[78] As explained earlier, the isopycnic surface causing the central flash was assumed to coincide with an isobaric
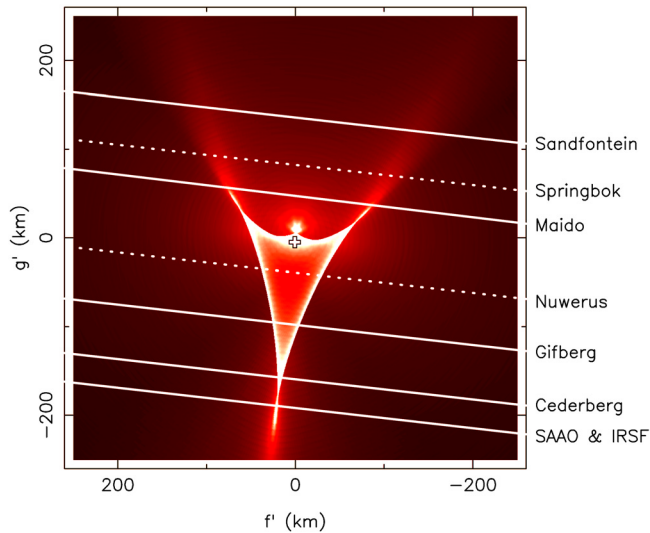
Figure 12. Two-dimensional map of the flash intensity in I band corresponding to the fit of Figure 11 ($\eta = 1.10$). The color scale is such that white is reached for regions where the stellar flux exceeds 80% of its unocculted value in I band. The brightest regions of the central flash, coded in white, delineate the so-called caustics, or evolute, and correspond to the centers of curvature of the limb causing the flash. The solid lines correspond to the tracks where the flashes were actually observed, while the dotted lines are the paths of the stations where observations were attempted but not successful due to bad weather. The black open cross is the shadow center derived from a circular fit to the inversion layer; see Figures 6 and 7. For the solution shown here, this center is displaced toward the south by 5 km with respect to the shadow center derived from the central flash fit; see Table 3. In the presence of fluctuations along the limb, the central flash can be modified; see Figure A2.

surface; i.e., this isopycnic surface is assumed to be isothermal. Consequently, zonal wind profiles can be deduced once the shape of the isopycnic surface is determined, through hydrostatic equilibrium (equation (6)). In reality, there are temperature contrasts ΔT between the equator and the poles, so that the isopycnic and isobaric surfaces diverge as higher latitudes are reached. The recent Composite Infrared Spectrometer (CIRS) measurements on board Cassini have shown, indeed, quite modest temperature contrasts (a few degrees at most) in the whole Titan's southern hemisphere at 0.25 mbar [see *Flasar et al.*, 2005], so that our hypothesis is valid for that hemisphere.

[79] In the northern hemisphere, however, the temperature contrast measured by CIRS reaches 5–10 K between the warmer equator and the cooler higher latitudes at ~55°N and 0.25 mbar level. The effect of meridional temperature contrasts on the zonal wind derivation was studied in detail by *Hubbard et al.* [1993]. It was found, for instance, that a contrast of $\Delta T = 17$ K between the equator and 77°.5 would increase by about 14% the zonal wind derived under the barotropic approximation. Consequently, scaling this result to the temperature contrasts observed in 2004 by CIRS, we can estimate that the barotropic approximation should not underestimate the jet by more than about 10% in the northern hemisphere. Giving more specific corrections and error bars on the value of the northern jet (in view of the discussion above) is difficult. First, because the CIRS results were obtained fourteen months after the occultation, so that the thermal map of the atmosphere may have changed. Second, the altitude we probe with the central flash (around 250 km) is at the upper limit where reliable results can be provided by CIRS. The 10% correction quoted above, however, remains small enough that it does not alter our conclusions below.

[80] The domain of zonal winds corresponding to $1.02 \leq \eta \leq 1.15$ is shown in Figure 13 (gray region), with our preferred value, corresponding to $\eta = 1.10$, drawn as a solid line. Basically, we obtain a very asymmetric profile, with a strong jet at the highest visible winter latitudes, about 215 m s^{-1} at 55°N in our preferred model, decreasing to about 150 m s^{-1} at the equator, and then tapering off to zero in the summer (southern) hemisphere. Even though we do not pretend that all the details of our wind profile are correct, one robust result is that there is a strong asymmetry between the northern and southern hemispheres in terms of wind intensity. This is clearly illustrated in Figures 11 and 12, where we see that two stations whose trajectories are symmetric with respect to Titan's shadow center (SAAO and Sandfontein), exhibit very different central flashes: a narrow spiky one at SAAO and a broad diffuse one at Sandfontein.

[81] Note that this asymmetry is also clearly visible in the limb profile (the blue curve in Figure 13), with an increase of about 50 km in radius for the isopycnal surface between the north pole and latitude 30°N, followed by a roughly circular limb between 30°N and the south pole.

[82] We emphasize here that the circularity found for the inversion layer at 515 km (section 3) is not inconsistent with the significant departure from sphericity found here at 250 km. First, note that the inversion layer is probed between latitudes 3°S and 11°N (see Table 2), where the altitude of the central flash layer varies by less than 0.5 km; see the blue curve in Figure 13. Second, note anyway that 265 km in altitude separate the two layers, i.e., more than five scale heights. There is no reason why the shape of the two layers should be identical with such a large separation. Actually, *Moreno et al.* [2005] do measure a decrease of the equatorial wind velocities from 160 ± 60 m s^{-1} at 300 ± 150 km altitude down to 60 ± 20 m s^{-1} at 450 ± 100 km altitude.

[83] Our profile is compared to wind profiles derived from the central flash analysis of 3 July 1989 [*Hubbard et al.*, 1993], from the 20 December 2001 occultations [*Bouchez*, 2004] and from the CIRS instrument during the second half of 2004 [*Flasar et al.*, 2005]. In terms of seasons at Titan, the northern summer solstice was reached in February 1988, the equinox occurred in November 1995, and the northern winter solstice was reached in November 2002.

[84] Thus the 28 Sgr occultation was observed about one and a half terrestrial years after northern summer solstice, and the 14 November 2003 occultations, about one year after northern winter solstice. These two sets of observations were thus taken essentially one-half Titan year apart. One sees in Figure 13 that the July 1989 southern jet (about 175 m s^{-1} at 65°S) is a rough reflection, with respect to the
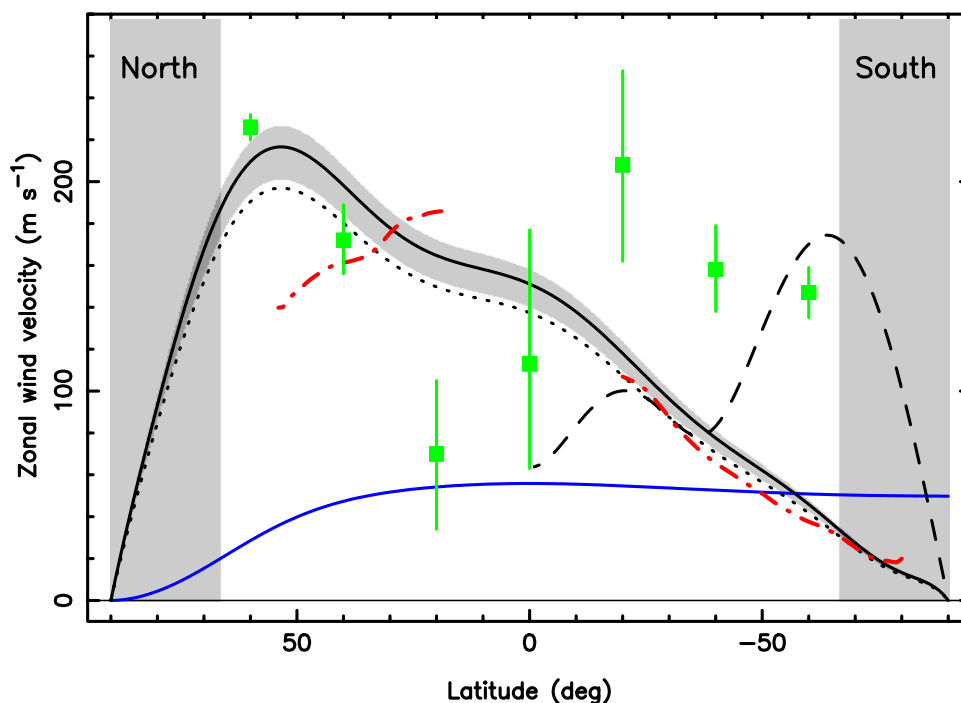
Figure 13. Zonal wind profile derived from our central flash analysis. We assume that the wind profile is deduced from *Rannou et al.*'s [2004] nominal profile, shown as a black dotted line, through a unique scaling factor η (equation (9)). Our preferred profile (black solid line) corresponds to $\eta = 1.10$, and the gray area around this curve corresponds to the confidence interval $1.02 \leq \eta \leq 1.15$ where acceptable fits are obtained; see text. The vertical gray boxes at right and left define the interval of latitudes (below 65.5°S and above 65.5°N) where no information is available, due to the tilt of the satellite with respect to the observer; see Figure 6. The blue curve shows the variation of radius Δr (in kilometers using the same scale as for the wind velocity) of a isopycnic level surface, corresponding to our preferred wind profile (the reference distance being the northern polar radius). Our profile is compared with other Titan zonal wind measurements. Black dashed line: profile obtained by *Hubbard et al.* [1993] from the 3 July 1989 28 Sgr occultation. It is limited to the southern hemisphere because thick hazes prevented the exploration of Titan's northern limb. Green squares with error bars: profile obtained by *Bouchez* [2004] from the 20 December 2001 stellar occultation. Red dash-dotted line: wind profile obtained from the CIRS instrument on board the Cassini orbiter during the second half of 2004 [*Flasar et al.*, 2005]. The interruption of the latter profile around the equator (between 19°S and 18°N) is caused by boundary condition constraints when resolving the thermal wind equation [*Flasar et al.*, 2005].

equator, of the 14 November 2003 northern jet, as expected since seasons have been swapped between the two hemispheres. Note that both profiles are derived from ground-based central flash observations, and thus can be consistently compared, although some differences exist in our fitting methods; see Appendix B. In any cases, both central flash analyses provide a consistent result, namely, a strong jet ($\sim$200 m s^{-1}) in the higher winter latitudes (50–60°), decreasing to $\sim$100–150 m s^{-1} at the equator.

[85] The 20 December 2001 zonal wind profile, in contrast, provides a more complex structure, with a strong jet ($\sim$225 m s^{-1}) at 60°N and another jet ($\sim$210 m s^{-1}) at 20°S; see the squares in Figure 13. The northern jet agrees well with what we see two years later, in November 2003. In contrast, the two profiles clearly disagree in the southern hemisphere, where we derive weaker winds. It remains to be seen whether this is evidence for a transient regime, where the southern activity, in terms of winds, damped down between 2001 and 2003, while the high northern latitudes were experiencing a steady strong jet.

[86] The CIRS profile shows a very good agreement with our profile in the southern hemisphere. In the northern hemisphere, however, the match is not so good, with a CIRS wind velocity peaking at 190 m s^{-1} near 18°N, and then decreasing to 140 m s^{-1} near 55°N, where we actually find a maximum velocity of about 215 m s^{-1}. This difference is larger than the error bars announced by *Flasar et al.* [2005] for their velocity profile, namely, less than about 5 m s^{-1} at 55°N and at the 0.25-mbar level. More CIRS observations are clearly needed, especially at high latitudes, to allow a direct comparison of our results.

[87] *Kostiuk et al.* [2001], using Doppler shift of ethane lines near 12 μm, deduce an average prograde equatorial wind of 210 ± 150 m s^{-1} in the 0.1–7.0 mbar pressure range ($\sim$110–300 km altitude). More recent measurements in 2003, using the same technique, yield again a prograde equatorial wind of 190 ± 90 m s^{-1} near 230 km (0.4-mbar level), i.e., about 20 km below the level we probe here [*Kostiuk et al.*, 2005]. Those values are consistent with the typical value of 150 m s^{-1} that we obtain around the equator in November 2003; see Figure 13. Recent observations
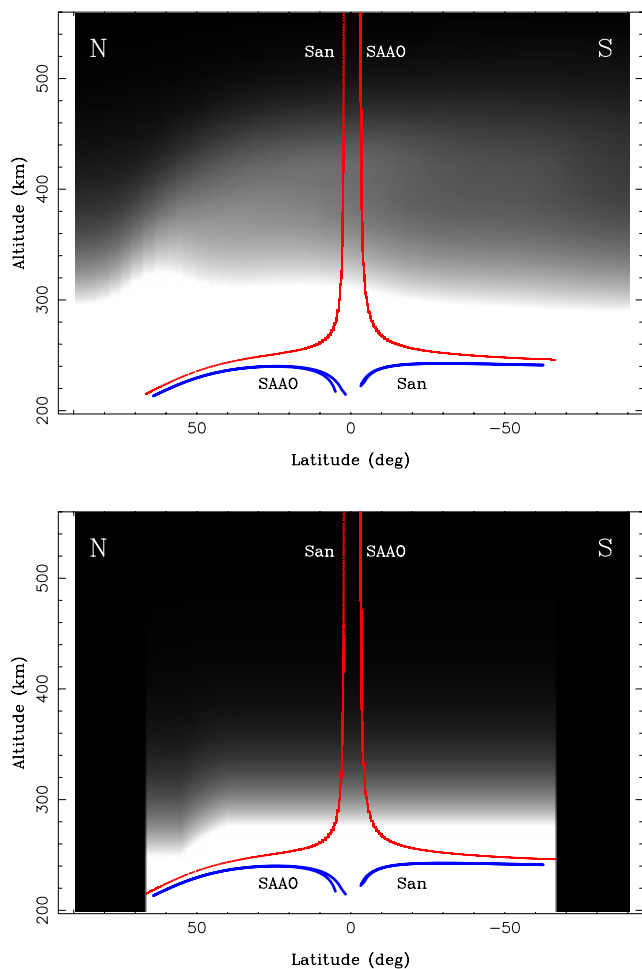
Figure 14. (top) The trajectories of the stellar images as observed from SAAO and Sandfontein. The gray scale shows the tangential optical depth τ (in I band) given in *Rannou et al.*'s [2004] model. The linear gray scale is such that white corresponds to $\tau \geq 1$, while black corresponds to $\tau = 0$. (bottom) Our best fit to the observations, inside the interval [65.5°S, 65.5°N]. Note that our results are valid only for those regions close to the tracks of the stellar images. Thus this image should not be interpreted as giving a 2-D view of Titan's aerosols distribution.

gathered by *Moreno et al.* [2005] in March 2003 and February 2004, using Doppler shift of CH_3CN lines at 1.35 mm, yield an integrated equatorial (and prograde) wind velocity of 160 ± 60 m s^{-1} at altitude 300 ± 150 km, a figure which is also consistent with our results at 250 km.

[88] Finally, *Luz et al.* [2005], using Doppler shift measurements in the UV, detect a prograde wind around the equator, with lower limits of 62 and 50 m s^{-1} at altitude levels centered at 200 and 170 km, respectively, a result consistent with all the profiles presented in Figure 13.

8. Spatial Distribution of Hazes

[89] Beyond informing us about the shape of the 0.25 mbar isobar, the central flash provides constraints on the aerosol distribution along all Titan's limb. This is due to the fact that the two stellar images (four inside the caustics) observed at each station scan almost all the visible latitudes during the occultation, at altitudes of roughly 240 km (Figures 10 and 14). At all those latitudes and all wavelengths, the flash is actually fainter than expected from a clear atmosphere. The quantities associated with very simple haze distribution described in section 6.1, namely, a thicker aerosol layer south of ϕ_{inf} and a clearer layer north of ϕ_{sup}, are given in Table 3. We can see a transition between a thicker haze south of $\phi_{inf} = 40°N$ to a thinner one north of $\phi_{sup} = 55°N$.

[90] This transition to a thinner haze at high latitudes is robustly constrained by the shape of the central flashes. In order to generate these flashes, we need the optical depths at both northern and southern latitudes. Since the fluxes (in a clear atmosphere) coming from the near- and far-limb images are comparable (see, e.g., Figure A3), and because a unique model must explain all the flashes analyzed here, we have no choice but to allow for this transition between 40°N and 55°N in order to simultaneously fit the data.

[91] Figure 14 compares our results with the haze expected from *Rannou et al.*'s [2004] GCM model. The upper panel shows the tangential optical depths expected from this model, while the lower panel shows our results. Although there is a good general agreement between the GCM and our results in the southern hemisphere, we clearly need a much more transparent atmosphere than predicted by the GCM at high northern latitudes. In particular, the northern polar hood present in the GCM is much too thick when confronted with our observations. Actually, with such a hood, we could never have detected the flashes. For instance the rays causing the flash at SAAO, and coming from the atmosphere around 65°.5N, should traverse tangential optical depths of more than seven (I band) according to the GCM. What we predict on the contrary is that the main haze layer clears up north of $\sim 55°N$, so that the tangential optical depth at 65°.5N and 220 km altitude, is only $\tau \sim 1.1$, versus $\tau \sim 2.1$ at 65°.5S and 240 km altitude.

[92] A similar result was obtained by *Hubbard et al.* [1993] from the July 1989 occultation, namely, a thicker haze in the summer (northern at that time) hemisphere, and a thinner haze in the winter (southern) hemisphere. The clearing in the haze layer was observed south of 24°S in July 1989 [*Hubbard et al.*, 1993], while the clearing we observe in November 2003 is north of $\sim 55°N$, i.e., closer to the pole than in 1989.

[93] The discrepancy between *Rannou et al.*'s [2004] GCM predictions for a northern polar hood and our result is surprising, considering the good agreement we obtain concerning the zonal wind regime, and remembering that there is a strong coupling between the haze distribution and the zonal wind profile. It is important to note, however, that we actually derive the haze optical depths only along the trajectories of the stellar images. Thus the lower panel of Figure 14 is somehow misleading in that it provides a 2-D interpretation of what is actually a 1-D information. In particular, a polar hood may exist above the high northern latitudes and still be consistent with our observations, as long as the tangential optical depth is about 1.1 in I band at the latitudes corresponding to the central flash, 65°.5N and at ~ 200 km altitude.
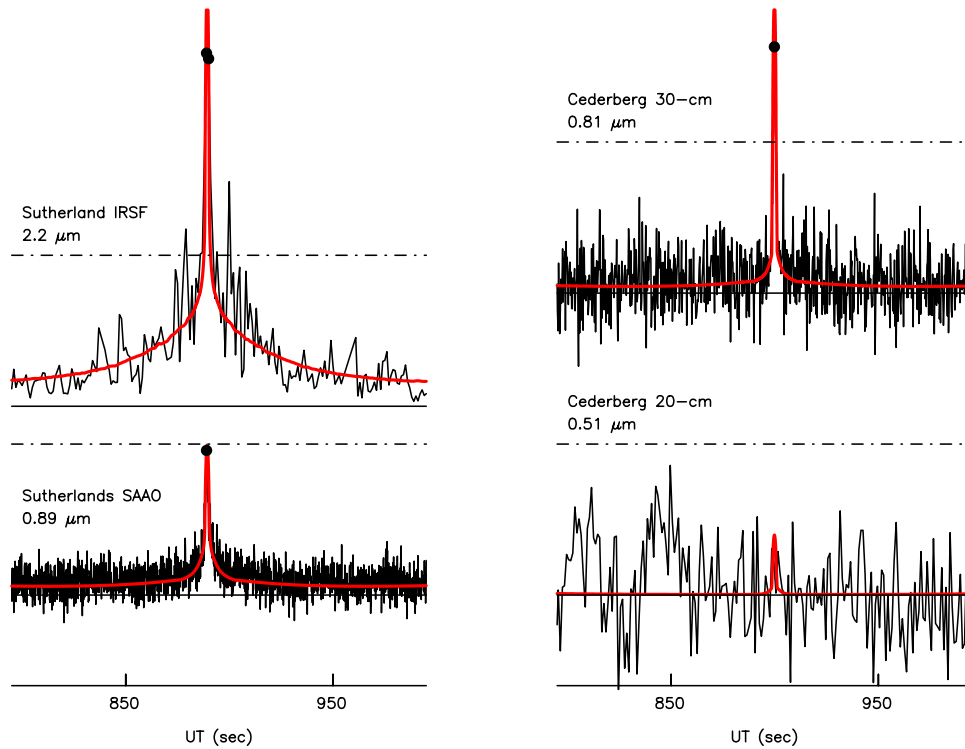
Figure 15. The central flash observed simultaneously in two colors (left) at Sutherland (2.2 μm and 0.89 μm) and (right) at Cederberg (0.81 μm and 0.51 μm). All the light curves are plotted at full time resolution, except for the Cederberg 20-cm data, which are smoothed at 1 s resolution. As in Figure 11, all the theoretical profiles have been smoothed with a smoothing parameter of $D_{\mathrm{sm}} = 24.6$ km. The calculated flashes (red curves) are generated with $\eta = 1.10$, a dependence $\tau \propto \lambda^{-1.7}$, and the other corresponding parameters of Table 3. Note that the central flash expected with the parameters used here is not detected, to within the noise level, at the Cederberg 20-cm telescope.

[94] In other words, a northern polar hood may exist, but it structure could be more complex than given by *Rannou et al.* [2004], with accumulation of dust above 300 km, but still modest optical depths at the levels we probe. Again, the Cassini results should discriminate between the various models for haze distribution above Titan's northern pole.

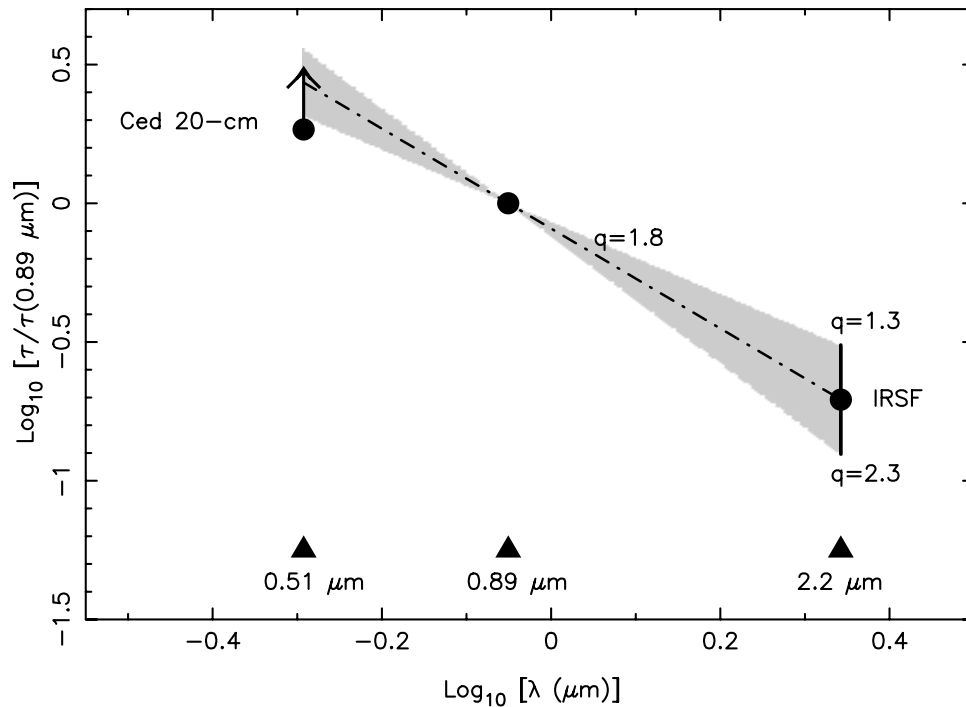## 9. Wavelength Dependence of Haze Opacity

[95] Data acquired at the same station, but in different bands, can constrain the wavelength dependence of the haze opacity near the 250 km altitude level. Two stations provide such multicolor data (see Table 1): (1) the SAAO site, with the 1-m telescope at $\lambda = 0.89$ μm and the IRSF 1.4-m telescope at $\lambda = 2.2$ μm, and (2) the Cederberg station, with the 30-cm telescope using $\lambda = 0.81$ μm and the 20-cm using $\lambda = 0.51$ μm.

[96] Note that all the other light curves examined so far were acquired between 0.7 and 0.89 μm, too narrow an interval to usefully constrain the wavelength dependence. Note also that we only use the central flashes in this comparison. Consequently, the results given in this subsection are relevant to the regions closest to the northern and southern poles of Titan, and for altitudes of about 240 km ($\sim$0.3 mbar). Practically, only the latitudes between $\sim$50°N and 65.5°N, and between $\sim$50°S and 65.5°S are concerned by this analysis.

[97] As mentioned earlier, we assume that the haze optical depth varies as $\tau \propto \lambda^{-q}$, where q is constant in all the wavelength domain covered here, namely, from 0.51 to 2.2 μm.

[98] The nominal case is given in Figure 15, where we have used the value $\eta = 1.10$ and $q = 1.7$, and the corresponding parameters given in Table 3. If q is decreased, everything equal besides, the flash will be more intense at 0.51 μm and more absorbed at 2.2 μm. Actually, the flash is *not* detected with the Cederberg 20-cm telescope at 0.51 μm because it is more absorbed than at 0.81 μm, and also because of the poorer signal to noise of this light curve (Figure 15). Consequently, this station only provides the lower limit $1.1 \leq q$. In contrast, the IRSF central flash provides both lower and upper limits for q: $1.5 \leq q \leq 2.1$. Thus the Cederberg 20-cm data are consistent with the IRSF data, but do not bring further information about the possible range for q.

[99] This result is applicable to the case $\eta = 1.10$, but is slightly changed for other values of η. Table 3 indicates that for the range of η considered here, $1.02 \leq \eta \leq 1.15$, we obtain an overall constraint of $q = 1.8 \pm 0.5$ from the observations made at 0.51, 0.89 and 2.2 μm, as illustrated in Figure 16. These results extend to the near IR the results that we obtained with the 28 Sgr occultation in 1989, for which a consistent value of $q = 1.7 \pm 0.2$ was obtained between 0.55 and 0.8 μm [*Hubbard et al.*, 1993]. As

Figure 16. Constraints on the wavelength dependence of the haze opacity at 250 km (0.25 mbar) based on the Cederberg (20-cm telescope) and Sutherland (IRSF) stations. The dash-dotted line corresponds to the median case $\tau \propto \lambda^{-q}$ with $q = 1.8$, and the gray zone delimits the possible solutions derived from our data, $1.3 \leq q \leq 2.3$. The Cederberg 20-cm telescope data only provide a lower limit for q, which is compatible with the IRSF constraint.

pointed out in that paper, the wavelength dependence can be used to constrain the haze particle sizes, a work that can now be extended to the near IR with the present results.

10. Concluding Remarks

[100] We have observed from four continents two stellar occultations by Titan on 14 November 2003. All the light curves exhibit a sharp feature at ingress and egress, which reveals the presence of a circular structure around Titan's limb, as outlined in Figure 6. This structure is actually a sharp inversion layer near 515 km altitude (1.5 μbar pressure level), where the temperature increases by 15 K in 6 km only (Figure 9). This layer is reminiscent of two other inversion layers observed deeper in the atmosphere (at 425 and 455 km, respectively) during the 3 July 1989 stellar occultation [*Sicardy et al.*, 1999]. This layer is actually present around 510 km in the Huygens HASI data taken on 14 January 2005 [*Fulchignoni et al.*, 2005], i.e., very close to the altitude we find fourteen months earlier. A careful comparison of our occultation results and the HASI profiles is now under progress to quantify the similarities, and possible differences, of these profiles.

[101] The central flashes observed during the first occultation provide an accurate shape for the isopycnic (isodensity) surface around 250 km (0.25 mbar). Assuming that this surface coincides with an isobar, we deduce the zonal wind profile which is necessary to maintain the departure of this surface from sphericity. We find that a wind regime which is a mere scaled version of that predicted by the GCM model of *Rannou et al.* [2004] can reproduce satis-

factorily all the observed flashes (Figure 11). Actually, the best wind profile is deduced from *Rannou et al.*'s [2004] predicted winds by a simple multiplicative factor of 1.10; see Figure 13. It remains to be seen whether other wind regimes with more complex shapes can also reproduce our observations. In any case, it is clear that the observed flashes require a very asymmetric wind regime in the northern and southern hemispheres, with stronger winds in the northern hemisphere. This is necessary to explain the strong differences in the flashes observed from stations which passed symmetrically north and south of Titan's shadow center.

[102] The haze distribution around Titan's limb at 250 km altitude is close to the one predicted by *Rannou et al.* [2004] in the southern hemisphere, but is quite different in the northern latitudes between ~40°N and 65°N. While the GCM model predicts a thicker and thicker polar hood as higher latitudes are probed, we actually observe a clearing north of 40°N (Figure 14). This does not mean that the polar hood does not exist, but rather, that it had a different structure than expected. Data from the Cassini orbiter will certainly help having a more consistent view of the hazes at these northern latitudes.

[103] Finally, simultaneous observations of the flashes at various wavelengths provide constraints on the wavelength dependence of haze opacities at 250 km altitude. We find that for λ between 0.51 and 2.2 μm, the tangential optical depth τ has a dependence $\tau \propto \lambda^{-q}$, with $q = 1.8 \pm 0.5$. This extends to the near IR the results that we obtained with the 28 Sgr occultation in 1989, which yielded a consistent value of $q = 1.7 \pm 0.2$ between 0.55 and 0.8 μm [*Hubbard et al.*,
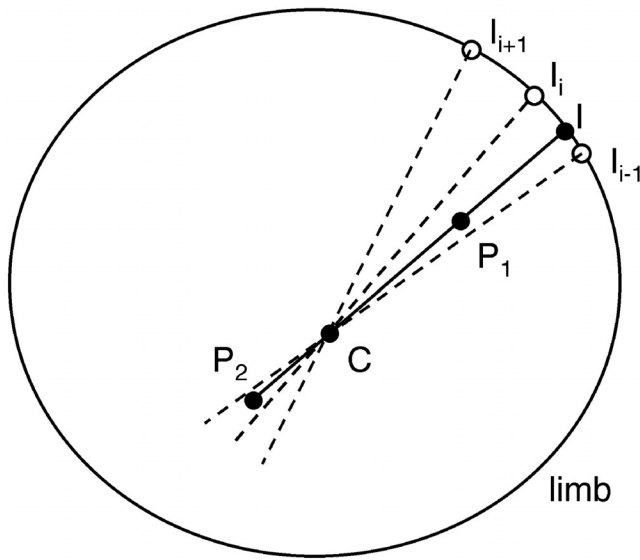
Figure A1. Geometric constructions to generate the central flash. See text for details.

1993]. Such results can now be used to constrain the aerosol particle sizes at that altitude.

[104] A work which clearly remains to be done now is a detailed comparison of all the light curves obtained during the two occultations of 14 November 2003. Such study will provide a fine vertical view of Titan's atmosphere between $\sim$300 and 500 km, with comparison over horizontal scales of a few tens of km up to about 500 km. This can yield good constraints on the structure of the gravity waves which seems to perturb Titan's upper stratosphere.

Appendix A: Generating the Central Flash

A1. Refraction

[105] The factor f_{ref} in equation (5) is calculated using ray tracing in a prescribed atmosphere, namely, the *Yelle* [1991] nominal model. From the Yelle density profile $n(z)$, we derive the refractivity $\nu(z)$, where $1 + \nu$ is the index of refraction. We assume a pure molecular nitrogen ($N2$) atmosphere, so that $\nu = K_{N2} \cdot n$, where the molecular refractivity of nitrogen K_{N2} is given by $K_{N2} = 1.091 \times 10^{-23} + 6.282 \times 10^{-26}/\lambda_{\mu m}^{2}$ cm^3 molecule^{-1} [*Washburn*, 1930]. Introducing a few percent of methane would not change significantly the atmospheric refractive index, so that this gas is not accounted for in our refraction model.

[106] The bending angle $\omega(r)$ suffered by the stellar ray which has a closest approach distance r to Titan's center is calculated by ray tracing, i.e., by integrating numerically the equation $\omega(r) = \int_{-\infty}^{+\infty} (r/x) \cdot (\partial\nu/\partial r)\, dx$ along the (almost rectilinear) trajectory of a photon in the atmosphere; see details and notations of *Sicardy et al.* [1999, Appendix B].

[107] We then obtain the normalized (between 0 and 1) flux at the distance $z = r + \omega\Delta$ from the shadow center, due to differential refraction, through $f_{ref} = 1/[1 + \Delta(\partial\omega/\partial r)]$, where Δ is the distance to Titan. To avoid artificial spikes in the light curve, we have to use a smooth spline interpolation of Yelle's model, in which we divide the atmosphere into 0.05-km thick layers between the altitudes 200 km and 1300 km.

[108] Yelle's model describes Titan's atmosphere at the equator, while the stellar images observed during the occultation explore all latitudes ranging from $\sim$65°.5S to 65°.5N, these limits being imposed by Titan's viewing geometry at the moment of the occultation (Figure 6). Note that a given isopycnic (constant density) layer can have altitude variations of $\sim$40 km (Figure 10). In order to take this effect into account, we shift vertically Yelle's profile by the corresponding amount, once the isopycnic shape is given.

A2. Ray Focusing

[109] As the stellar image probes Titan's atmosphere, it is squeezed perpendicular to the limb by the factor $f_{ref} < 1$, due to differential refraction. At the same time, it is stretched along the limb by the factor $f_{foc} > 1$, due to the limb curvature.

[110] Let I denote the position of the stellar image in the plane of the sky, and let the "limb" denote the projection in the plane of the sky of the isopycnic level going through I (Figure A1). Then if C is the center of curvature of the limb at I and P is the position of the observer projected in the plane of the sky, we have $f_{foc} = CI/CP$, from conservation of energy.

[111] Near the center of Titan's shadow, CP is small, so that f_{foc} gets large, yielding the so-called central flash region. The flux actually diverges to infinity on the set of centers of curvature C, called the caustics, or evolute (the bright boundary of the central flash region, coded in white in Figure 12). The layer in Titan's atmosphere responsible for the caustics will be called herein the "central flash layer." It lies typically at 0.25 mbar, corresponding to a typical altitude of 250 km at the equator, and 200 km at the north pole; see Figure 10.

[112] Note that the central flash layer is very thin. Due to the squeezing of the stellar image evoked above, and
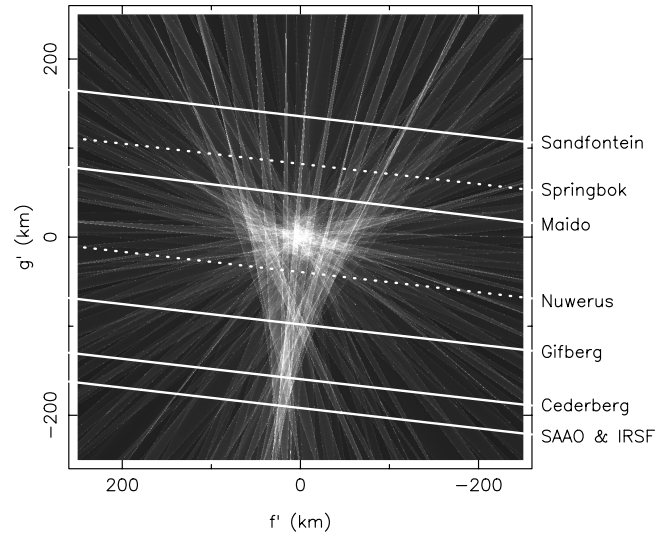
Figure A2. Central flash map in the presence of irregularities along the limb drawn in Figure A1; see Appendix A for details. This map is to be compared with the one in Figure 12, obtained with a smooth limb. The scatter of the centers of curvature causes the spreading of the central flashes; see an example in Figures A3 and A4.
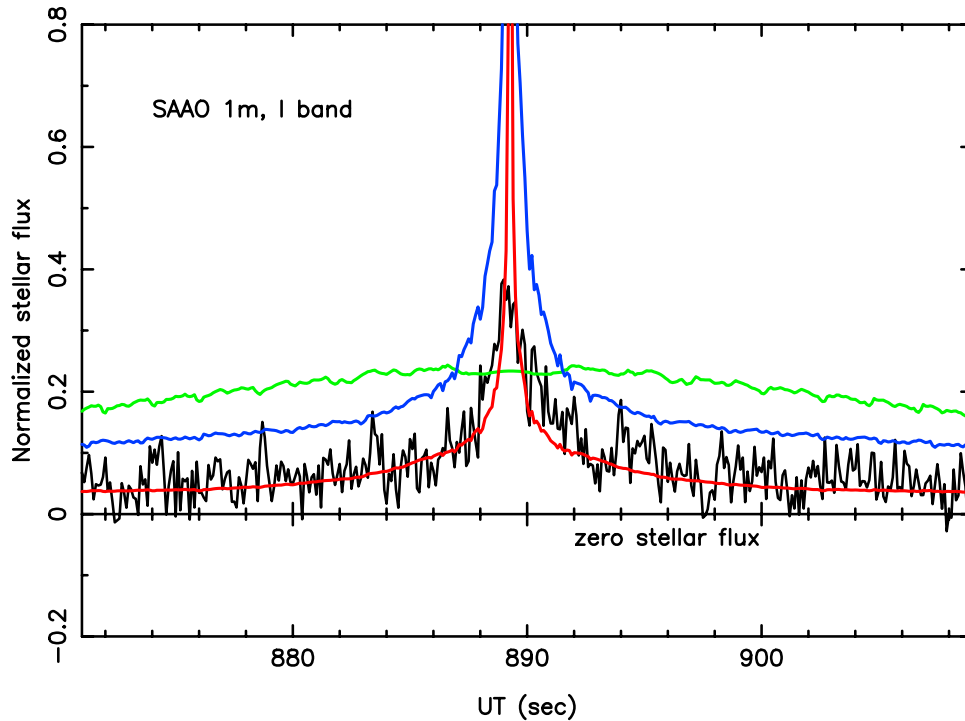
Figure A3. Example of a fit to the SAAO 1-m central flash (black curve). We use here the nominal [*Rannou et al.*, 2004] zonal wind profile multiplied by $\eta = 1.10$, and a correction to the impact parameter of $\Delta g'' = +5.0$ km; see Table 3. The fluxes have been normalized between zero (complete disappearance of the star) and unity (corresponding to the unocculted stellar flux). The green (resp. blue) solid line is the expected flux from the primary (resp. secondary) stellar image, coming from the southern (resp. northern) limb, if the atmosphere were transparent. The small fluctuations observed in the model are caused by the discrete layers (50 m in height) used for calculating the vertical refraction of the stellar rays in Titan's atmosphere; see Appendix A. The red solid line is a linear combination of the primary and secondary fluxes, smoothed by a stellar diameter of 2.2 km projected at Titan. This combination is obtained with a optical depth (along the line of sight) of $\tau_{sup} = 1.1$ for titanocentric latitudes $\phi \geq \phi_{sup} = 55°$N and $\tau_{inf} = 2.2$ for latitudes $\phi \leq \phi_{inf} = 40°$N. These optical depths have been adjusted so that the derived flash (red curve) has the same area as the data (black curve). The calculated flash is too narrow compared to the data, so that a further smoothing is needed to fit the observations; see Figure A4.

considering that the refractive factor is only $f_{ref} \sim 10^{-2}$ near the shadow center, this means that the central flash layer has a thickness of f_{ref} times the stellar diameter projected at Titan (2.2 km for the star of the first occultation), i.e., a small fraction of km. Consequently, the central flash light comes from a very limited region of the atmosphere, so that it is not necessary to model the shape of the whole atmosphere, but only of the central flash layer.

[113] To derive the shape of the caustics, we proceed as follows:

[114] 1. We start from a prescribed shape for the central flash layer, as detailed later. We assume that this layer is axisymmetric and aligned with Titan's spin axis. Consequently, the radius of that layer depends only upon latitude.

[115] 2. We project that layer onto the plane of the sky, using the planetocentric elevation of the observer, B, and the position angle P of Titan's spin axis projected onto the sky plane; see section 3. This intersection is called the central flash limb, or simply the limb.

[116] 3. We calculate the caustics caused by that limb. For this, we sample the limb at regular (one degree) intervals. Three adjacent points on the limb bracketing I then pertains to a unique circle, whose center C is considered as the

center of curvature of the middle point, I. The line joining I to C is called a radius.

[117] 4. For any observer lying at point P in the shadow, we can calculate the number of images produced by the limb and their respective focusing factor f_{foc}. For this, it is enough to look to for those radii which encompass the point P, and then take $f_{foc} = CI/CP$. The image of the star is qualified as primary (or near limb) if P lies between C and P. For instance, I is a primary image for an observer at P_1 in Figure A1. The image is said to be secondary (or far limb) if C lies between P and I. Thus I is a secondary image for an observer at P_2. Far from the central flash region, there are two images (one primary and one secondary). Two images (one primary and one secondary) appear or disappear every time the caustics is crossed, so that there can be 2, 4, 6... images visible along the limb at a given moment.

A3. Scintillation

[118] The procedure described above does not take into account the possible effects of scintillation on the central flash shapes. Examples of scintillations are clearly visible in the IRSF central flash; see Figure 15. As discussed in section 6.2, this scintillation can be responsible for the
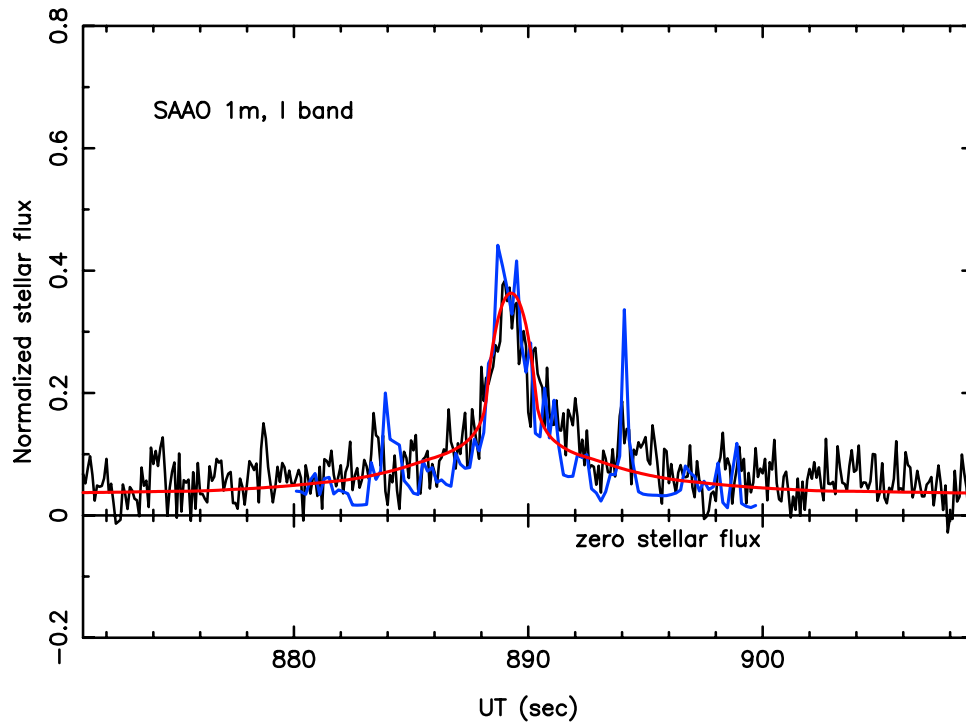
Figure A4.   Blue curve: calculated flash obtained with the same parameters (optical depths and stellar diameter) as in Figure A3, but with small height fluctuations (300 m r.m.s.) added to the altitude of the central flash layer; see details in Appendix A. These fluctuations spread out the flash (red curve in Figure A3) while conserving the total amount of light in the central flash region. The spikes in the model (in particular the one near 894 s UT) are random features caused by local focusings of light associated with the height fluctuations added to the flash layer; see examples in Figure A2. Red curve: Because the generation of the blue curve is time consuming, we have fitted the central flash by using the smooth red curve of Figure A3 and by convolving that model with an equivalent stellar diameter of $D_\star$ = 24.6 km, i.e., more than ten times the actual stellar diameter projected at Titan; see section 6.2 and Appendix A for details.

spreading of the flashes well beyond the spreading effect of the stellar diameter.

[119]   An illustration of this effect is given in Figure A2. The smooth limb shown in Figure A1 has been radially distorted, so that the isopyc layer causing the flash is submitted to small amplitude (typically ±300 m) altitude fluctuations through a random superimposition of waves with horizontal wavelengths (along the limb) ranging from 170 to 1050 km. Due to the irregularities of the limb, the centers of curvature are scattered around the evolute expected from a smooth limb (see Figure 12). This scatter has the effect of spreading each central flash, while conserving the total amount of light in the central flash region. This is illustrated in Figures A3 and A4. See also section 6.2 for discussion.

[120]   The calculation of the flash profiles in the presence of scintillation is time consuming from a computational point of view, since it requires a dense mesh in the ray tracing procedure. To remedy this problem, we have approximated the spreading effect of scintillation by the smoothing by an uniform disk of diameter D_{sm} in the shadow plane, a much faster procedure, since its require a sparser ray tracing. We have verified that a unique value of D_{sm} (here 24.6 km) is sufficient to reproduce the effect of

scintillation at the stations were the evolute was crossed (SAAO, Cederberg, Gifberg and Maïdo). Thus D_{sm} is a unique and global parameter which satisfactorily represents the spreading effect of scintillation.

A4.   Absorption

[121]   Each stellar image I visible by an observer at point P lies at a certain latitude ϕ and a certain altitude z above Titan's surface. Using some prescribed model for the vertical haze distribution (see section 6.1), we get the tangential optical depth $\tau(\phi, z)$. The corresponding attenuation to apply to the stellar flux is $\exp(-\tau)$, so that the observed stellar flux becomes $F_\star = f_{ref} \times f_{foc} \times \exp(-\tau)$. Finally, the fluxes from all the images (primary and secondary) I seen by P are added to get the total stellar flux detected by P.

Appendix B: Fits to the Data—Procedure

[122]   In order to systematically explore the effect of the various parameters to the final fit, we proceed as follows.

[123]   Step 1: We assume that the wind profile is a scaled version of the *Rannou et al.* [2004] zonal wind field; see
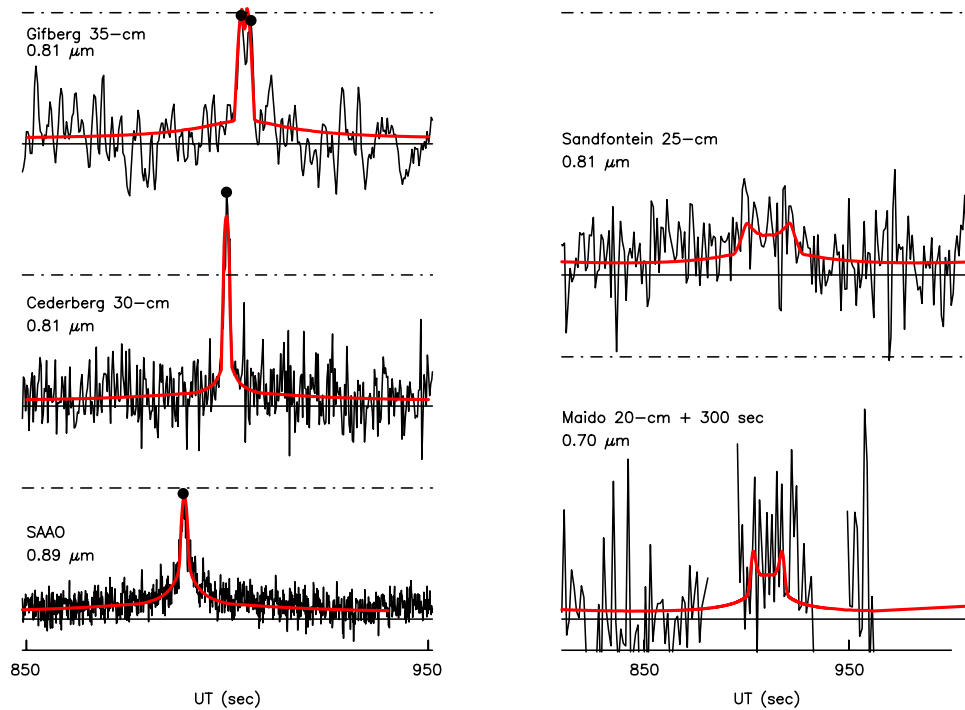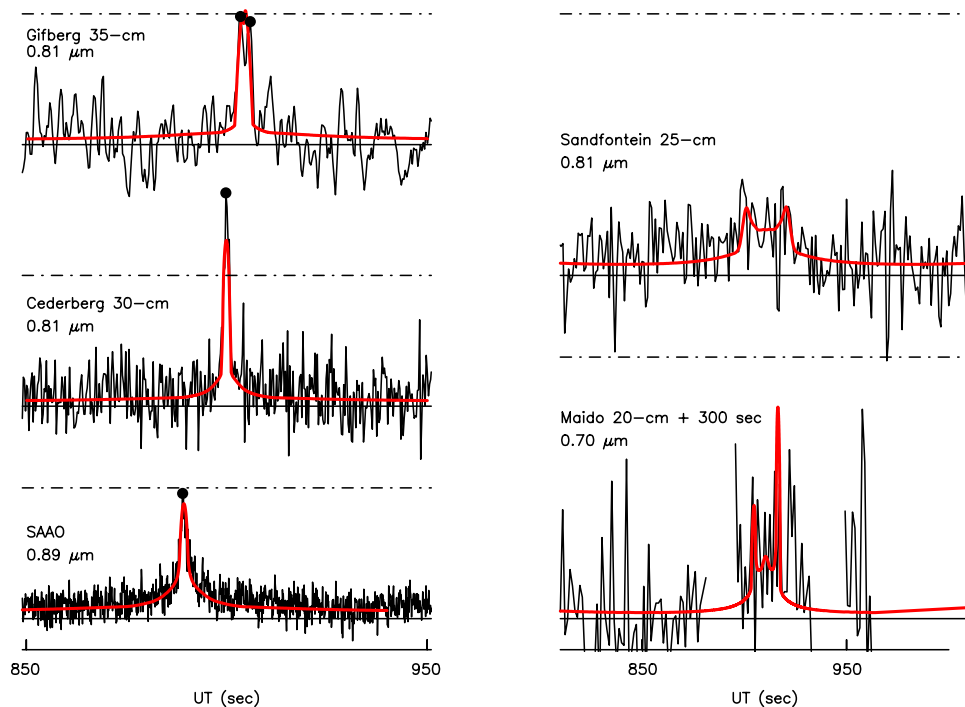
Figure B1. Same as Figure 11, but with $\eta = 1.02$.

equation (9) and the associated discussion. We then generate numerically the limb shape using equation (7).

[124] Step 2: We use some given initial values for the N-S shift $\Delta g''$ and the smoothing parameter D_{sm}. We then apply the ray tracing method described in the previous section to generate the light curve at the SAAO station, assuming a transparent atmosphere. Doing so, we store separately the contributions of the near and far-limb images; see Figure A3. The choice of the SAAO station is justified by the fact that it provides the best calibrated and highest SNR data, among all the available data here.

[125] Step 3: The optical depths τ_{sup} and τ_{inf} are adjusted so that the calculated flash matches the SAAO observed flash. This is feasible because the SAAO central flash has

Figure B2. Same as Figure 11, but with $\eta = 1.15$.

comparable contributions from both the southern and northern limb stellar images, making the adjustment robust. Typical values are $\tau_{sup} \sim 1$ and $\tau_{inf} \sim 2$ in the I band (Table 3).

[126] At that point, the smoothing parameter D_{sm} is generally not adequate, and the procedure is resumed at Step 2 with a different value of D_{sm} until a satisfactory fit to the SAAO data is obtained. The best fit is obtained with $D_{sm} \sim 24.6$ km, whatever the other parameters of the fits are. This diameter corresponds to a duration of 2.1 s in the shadow plane, comparable to the typical flash duration; see Figure A3. Thus the smoothing by D_{sm} is quite significant.

[127] Step 4: Using the optical depths derived in Step 3, we generate the central flash expected at Cederberg (0.81 μm). Usually the astrometric solution is not adequate, so that we have to change the value $\Delta g''$, then resuming Steps 2 to 4 until a satisfactory fit to both the SAAO and Cederberg data is obtained. This fit is generally obtained when the SAAO trajectory grazes the southern tip of the central flash caustics, see Figure 12.

[128] Step 5: We calculate the central flash at Gifberg. At that point, it is necessary to adjust the boundary latitudes ϕ_{sup} and ϕ_{inf} delimiting the denser and the clearer hazy regions in order to fit the Gifberg flash. As said before, we need a rather sharp transition between the two regions, somewhere between 40°N and 55°N. This means that in this interval of latitudes, the relatively opaque ($\tau \sim 2$ in the I band) main haze layer which prevails in the southern hemisphere up to mid-northern latitudes is replaced by a semitransparent layer ($\tau \sim 1$) when approaching Titan's northern regions.

[129] This adjustment of ϕ_{sup} and ϕ_{inf} also improves the shapes of the SAAO and Cederberg flashes because they help creating sharper flashes, especially at Cederberg where the observed flash is very sudden, with no broad wings before and after the flash (Figure 11). This sharpness is due to the fact that the stellar image moving toward higher northern latitudes suddenly emerges from behind the denser haze layer at it move north of ϕ_{sup}.

[130] Step 6: Most of the flashes are observed in the domain 0.70–0.89 μm (Table 1). We use two flashes observed at different wavelengths, namely, at 0.51 μm with the 20-cm telescope at Cederberg, and at 2.2 μm with the IRSF 1.4-m telescope at Sutherland, to constrain the dependence of opacity with wavelength. This step is explained in more detail in section 9.

[131] Step 6 completes our fit procedure for a given value of η. Other values of η can be used, resuming the procedure from Step 1.

[132] Examples of fits to the data are given in Figures B1 and B2 with some extreme acceptable values for η. The best fit we obtained is given in Figure 11; see the main text for details and comments.

References

Bouchez, A. (2004), Seasonal trends in Titan's atmosphere: Haze, wind, and clouds, Ph.D. thesis, Calif. Inst. of Technology, Pasadena. (Available at http://www2.keck.hawaii.edu/optics/staff/abouchez/thesis/)

Elliot, J. L., M. J. Person, and S. Qu (2003), Analysis of stellar occultation Data. II. Inversion, with application to Pluto and Triton, *Astron. J.*, *126*, 1041–1079.

Flasar, F. M., et al. (2005), Temperatures, winds, and composition in the Saturnian system, *Science*, *307*, 1247–1251.

Fulchignoni, M., et al. (2005), Titan's physical characteristics measured by the Huygens Atmospheric Structure Instrument (HASI), *Nature*, *438*, 785–791.

Hubbard, W. B., E. Lellouch, B. Sicardy, A. Brahic, F. Vilas, P. Bouchet, R. A. McLaren, and C. Perrier (1988), Structure of scintillations in Neptune's occultation shadow, *Astrophys. J.*, *325*, 490–502.

Hubbard, W. B., et al. (1993), The occultation of 28 SGR by Titan, *Astron. Astrophys.*, *269*, 541–563.

Kostiuk, T., K. E. Fast, T. A. Livengood, T. Hewagama, J. J. Goldstein, F. Espenak, and D. Buhl (2001), Direct measurement of winds of Titan, *Geophys. Res. Lett.*, *28*, 2361–2364.

Kostiuk, T., T. A. Livengood, T. Hewagama, G. Sonnabend, K. E. Fast, K. Murakawa, A. T. Tokunaga, J. Annen, D. Buhl, and F. Schmlling (2005), Titan's stratospheric zonal wind, temperature, and ethane abundance a year prior to Huygens insertion, *Geophys. Res. Lett.*, *32*, L22205, doi:10.1029/2005GL023897.

Lindal, G. F., G. E. Wood, H. B. Hotz, D. N. Sweetnam, V. R. Eshleman, and G. L. Tyler (1983), The atmosphere of Titan—An analysis of the Voyager 1 radio occultation measurements, *Icarus*, *53*, 348–363.

Luz, D., T. Civeit, R. Courtin, J. P. Lebreton, D. Gautier, P. Rannou, A. Kaufer, O. Witasse, L. Lara, and F. Ferri (2005), Characterization of zonal winds in the stratosphere of Titan with UVES, *Icarus*, *179*, 497–510.

Moreno, R., A. Marten, and T. Hidayat (2005), Interferometric measurements of zonal winds on Titan, *Astron. Astrophys.*, *437*, 319–328.

Narayan, R., and W. B. Hubbard (1988), Theory of anisotropic refractive scintillation—Application to stellar occultations by Neptune, *Astrophys. J.*, *325*, 503–518.

Rannou, P., F. Hourdin, C. P. McKay, and D. Luz (2004), A coupled dynamics-microphysics model of Titan's atmosphere, *Icarus*, *170*, 443–462.

Roques, F., et al. (1994), Neptune's upper stratosphere, 1983–1990: Ground-based stellar occultation observations III. Temperature profiles, *Astron. Astrophys.*, *288*, 985–1011.

Sicardy, B., et al. (1999), The structure of Titan's stratosphere from the 28 Sgr occultation, *Icarus*, *142*, 357–390.

Tracadas, P. W., H. B. Hammel, J. E. Thomas-Osip, J. L. Elliot, and C. B. Olkin (2001), Probing Titan's atmosphere with the 1995 August stellar occultation, *Icarus*, *153*, 285–294.

van Belle, G. T. (1999), Predicting stellar angular sizes, *Publ. Astron. Soc. Pac.*, *111*, 1515–1523.

Vervack, R. J., B. R. Sandel, and D. F. Strobel (2004), New perspectives on Titan's upper atmosphere from a reanalysis of the Voyager 1 UVS solar occultations, *Icarus*, *170*, 91–112.

Vienne, A., and L. Duriez (1995), TASS1.6: Ephemerides of the major Saturnian satellites, *Astron. Astrophys.*, *297*, 588–605.

Washburn, E. W. (1930), *International Critical Tables of Numerical Data: Physics, Chemistry and Technology*, vol. 7, p. 11, McGraw-Hill, New York.

Yelle, R. V. (1991), Non-LTE models of Titan's upper atmosphere, *Astrophys. J.*, *383*, 380–400.

————————

D. Baba, T. Nagata, and T. Nagayama, Department of Astrophysics, Nagoya University, Chikusa-ku, Nagoya 464-8602, Japan.

K.-L. Bath, W. Beisker, F. Bode, H.-J. Bode, M. Kretlow, H. Lüdemann, J. Lüdemann, D. Neubauer, A. Tegtmeier, C. Tegtmeier, and B. Thomé, International Occultation Timing Association, European Section, Hannover, Germany.

A. Bellucci, S. Lacour, J. Lecacheux, E. Lellouch, S. Pau, S. Renner, F. Roques, B. Sicardy, and T. Widemann, LESIA, Observatoire de Paris, Bâtiment 10, F-92195 Meudon Cédex, France. (bruno.sicardy@obspm.fr)

F. Colas and A. Fienga, Observatoire de Paris, IMCCE, 77 Avenue Denfert Rochereau, F-75014 Paris, France.

C. deWitt, B. Fraser, A. Jansen, T. Jones, P. Schoenau, and C. Turk, Astronomical Society of Southern Africa, P.O. Box 9, Observatory 7935, South Africa.

C. Etienne, Observatoire de Paris, CERCOM, 5 Place Jules Janssen, F-92195 Meudon Cédex, France.

F. Ferri, CISAS "G. Colombo", Università di Padova, Via Venezia 15, I-35131 Padova, Italy.

D. Fiel, Lycée Stanislas, 22 Rue Notre-Dame des Champs, F-75006 Paris, France.

E. Frappa, Astronef, Planétarium de Saint-Etienne, F-42100 Saint-Etienne, France.

I. S. Glass, South African Astronomical Observatory, P.O. Box 9, Observatory 7935, Cape Town, South Africa.

S. Itting-Enke, P.O. Box 5198, Windhoek, Namibia.

M. Hernandez, Association Aude, c/o F. Colas, 45 Avenue Reille, F-75014 Paris, France.

G. Hesler and T. Payet, ARECA, Sainte-Marie, La Réunion, France.

R. R. Howell, Wyoming InfraRed Observatory, Department of Physics and Astronomy, Department 3905, Laramie, WY 82070, USA.

F. Hund, Hakos Guestfarm, P.O. Box 5056, Windhoek, Namibia.

M. Kidger, Instituto de Astrofísica de Canarias, c/Vía Láctea s/n, E-38200, La Laguna, Tenerife, Spain.

C. Martinez, Instituto Superior de Ciencias Astronómicas, and Liga Iberoamericana de Astronomía, Simbron 3058, Capital Federal, Buenos Aires, Argentina.

P. Meintjies, Boyden Observatory, University of the Free State, P.O. Box 339, Bloemfontein, 9300, South Africa.

O. Naranjo and P. Rosenzweig, Universidad de Los Andes, Facultad de Ciencias, Departamento de Física, Grupo de Astrofísica Teórica, Mérida, Venezuela.

J. L. Ortiz, Instituto de Astrofísica de Andalucía, CSIC Apt. 3004, E-18080 Granada, Spain.

A. Peyrot, J. P. Teng, and M. Vignand, Observatoire Les Makes, La Rivière, La Réunion, France.

M. Rapaport, Observatoire Aquitain des Sciences de l'Univers, F-33270 Floirac, France.